

# Chemical abundances of planetary nebulae from optical recombination lines – I. Observations and plasma diagnostics

Y. Liu,<sup>1,2\*</sup> X.-W. Liu,<sup>1</sup> S.-G. Luo<sup>1</sup> and M. J. Barlow<sup>3</sup>

<sup>1</sup>Department of Astronomy, Peking University, Beijing 100871, China

<sup>2</sup>Center for Astrophysics, Guangzhou University, Guangzhou 510400, China

<sup>3</sup>Department of Physics and Astronomy, University College London, Gower Street, London WC1E 6BT

Accepted 2004 June 22. Received 2004 June 22; in original form 2004 April 26

## ABSTRACT

We have obtained deep optical spectra of medium resolution for a sample of 12 Galactic planetary nebulae (PNe). Optical recombination lines (ORLs) from carbon, nitrogen and oxygen have been detected in 11 of them and neon ORLs in nine of them. All spectra were obtained by scanning a long slit across the nebular surface, yielding relative line intensities for the entire nebula that are suitable for comparison with integrated line fluxes measured in other wavelength regions using space-borne facilities, such as the *Infrared Space Observatory* (ISO) and the *International Ultraviolet Explorer* (IUE). For 11 PNe, ISO infrared spectra between 2.4 and 197  $\mu\text{m}$  are available, most of them taken by ourselves, plus a *Kuiper Airborne Observatory* (KAO) infrared spectrum of NGC 6210. IUE ultraviolet (UV) spectra are available for all nebulae except one in our sample. The UV, optical and infrared spectra have been combined to study nebular thermal and density structures and to determine elemental abundances.

We have determined UV to optical extinction curves towards these PNe by examining observed fluxes of H I and He II recombination lines, radio free-free continuum flux density, and UV to optical nebular continua. For 11 PNe in our sample, the derived optical reddening curves are found to be consistent with the standard Galactic extinction law for a total-to-selective extinction ratio,  $R \equiv A(V)/E_{B-V} = 3.1$ . However, the optical extinction curve towards Hu 1–2 yields  $R = 2.0$ . The UV extinction towards Hu 1–2 and NGC 6572 is also found to be much steeper than the standard Galactic reddening law. In contrast, the UV extinction curve along the sight lines towards NGC 6210 is found to be much shallower, although in the latter case the uncertainties involved are quite large.

Electron temperatures and densities have been derived using a variety of diagnostic ratios of collisionally excited lines (CELs) in the UV, optical and infrared. The results show clear stratifications, both in temperature and density. Lines emitted by ions formed in regions of higher ionization degree yield higher temperatures than lines arising from regions of lower ionization degree, while densities deduced from ratios of infrared diagnostic CELs of low critical densities, such as the [O III] 88- $\mu\text{m}$ /52- $\mu\text{m}$  ratio, are systematically lower than those derived from UV and optical diagnostic lines, which in general have much higher critical densities than the infrared fine-structure lines.

Electron temperatures have also been derived from the ratio of the nebular continuum Balmer discontinuity to H 11 for 11 PNe. For four of these, the Balmer jump temperatures are more than 1000 K lower than values derived from the [O III] optical collisionally excited diagnostic line ratio. With a difference of 3580 K, NGC 40 has the lowest Balmer jump temperature relative to the [O III] optical forbidden-line temperature. High-order Balmer line decrements

\*E-mail: liuyi@bac.pku.edu.cn

have been used to determine electron densities. The results are consistent with values derived from forbidden-line density-diagnostics.

**Key words:** ISM: abundances – planetary nebulae: general.

## 1 INTRODUCTION

This paper is the first part of a work devoted to the study of chemical abundances for a sample of Galactic planetary nebulae (PNe) which, together with the second part (Liu et al. 2004, hereafter Paper II), aims at a better understanding of two fundamental problems in nebular astrophysics. One is the dichotomy of abundance determinations whereby heavy element abundances relative to hydrogen derived from weak optical recombination lines (ORLs; such as C II  $\lambda$ 4267, N II  $\lambda$ 4041, O II  $\lambda$ 4089, Ne II  $\lambda$ 4391) are systematically higher than those deduced from (much brighter) collisionally excited lines (CELs; most of them are forbidden lines). The other is the dichotomy of temperature determinations whereby for a given nebula the electron temperature derived from the Balmer jump of the H I recombination spectrum is systematically lower than the value derived from the traditional method using the collisionally excited [O III] forbidden-line ratio  $(\lambda 4959 + \lambda 5007)/\lambda 4363$  (see Liu 2002, 2003, for recent reviews).

The magnitudes of discrepancies between the nebular electron temperatures and heavy element abundances derived from recombination lines/continua, on the one hand, and those determined from CELs, on the other, are found to vary from nebula to nebula. Analyses so far have been focused on a small group of PNe which exhibit extremely rich and prominent ORL spectra, such as NGC 7009 (Liu et al. 1995), NGC 6153 (Liu et al. 2000), M 1–42 and M 2–36 (Liu et al. 2001b) and Hf 2–2 (Liu 2003). Careful nebular analyses of these extreme PNe have yielded recombination line C/Ne abundances that are often over an order of magnitude higher than the corresponding CEL values. For a given nebula, the relative abundances of heavy elements, such as the C/O, N/O and Ne/O abundance ratios derived from ORLs, are compatible with those obtained from CELs. The analyses show that both types of dichotomy are real and correlate with each other. In other words, the discrepancy between the ORL and CEL temperatures increases with the discrepancy between the ORL and CEL abundances (Liu et al. 2001b). Thus, they are most likely caused by astrophysical effects rather than uncertainties in observations or in the basic atomic physics. Detailed analyses also show that their more than a factor of 10 discrepancies between abundances derived from the two types of emission line cannot be explained by the hypothetical temperature fluctuations or density inhomogeneities that may be present in nebulae. Instead, it is suggested that these extreme PNe may contain another ionized gas component highly enriched in heavy elements. This component has a  $T_e$  of only a few hundred Kelvin (because cooling by the heavy element infrared (IR) fine-structure lines is then alone sufficient to balance the nebular heating rate) and emits strongly in heavy elemental ORLs but essentially none in CELs (Liu et al. 2000; Liu 2003).

Nebulae with abundance discrepancies over a factor of 5 are relatively rare. Amongst the limited number of PNe analysed so far, the discrepancies amount to a factor of 2 on average. It is currently un-

clear whether these moderate discrepancies can be explained within the paradigm of temperature fluctuations (Peimbert 1967; Ruiz et al. 2003) and density inhomogeneities (Rubin 1989; Viegas & Clegg 1994) or, as postulated in the cases of those extreme PNe showing very large abundance determination discrepancies, they are caused by contaminations of a previously unsuspected component of ionized gas of very low electron temperature and very high metallicity. To better understand and quantify these two fundamental problems in nebular astrophysics, it is clear that we need to analyse a large sample of PNe, in order to determine the magnitudes and distribution of the discrepancies and their possible correlations with other nebular and ionizing source properties, such as the morphology, abundances and kinematics of the nebula and the luminosity, effective temperature and surface composition of the ionizing star. For this purpose, we have obtained deep optical spectra for a large sample of Galactic PNe. 12 PNe from this data set have been analysed by Tsamis et al. (2003, 2004). In the current work, we present observations and analyses for another 12 PNe from this sample.

The observational data analysed in the current work are unique in two aspects. (i) All the optical spectra have been obtained by uniformly scanning a long slit across the nebular surface, thus yielding average line fluxes for the entire nebula that are suitable for comparison with integrated nebular fluxes measured with space-borne facilities, such as the *Infrared Space Observatory (ISO)* in the IR and the *International Ultraviolet Explorer (IUE)* in the ultraviolet (UV). (ii) For nearly all the nebulae, supplementary IR spectra from 2.4 to 197  $\mu$ m have been secured, most of them by our group, using the Short Wavelength Spectrometer (SWS) and Long Wavelength Spectrometer (LWS) on board *ISO*, which yield fluxes for many fine-structure lines. Together with the UV spectra, available for almost all of them from the *IUE* data archive, the current data set enables us to constrain nebular thermal and density structures and to determine elemental abundances using a variety of ionic emission lines of different characteristics (emission mechanisms, excitation energy and critical density, etc.). The inclusion of UV and IR data significantly increases the number of ionic species detected for individual heavy elements, and thus the accuracy of abundance determinations. More importantly, such multiwaveband analyses are essential in order to differentiate the various interpretations of the underlying causes of the aforementioned two fundamental problems in nebular astrophysics.

In this paper, we present deep, long-slit, scanned optical spectra for 12 Galactic PNe. We have detected ORLs from C, N and O ions in 11 PNe. ORLs from neon ions have been detected in nine of them. For the fainter NGC 6781, only the C II  $\lambda$ 4267 ORL has been detected. We present an extensive list of detected emission lines, including numerous C II, N II, O II and Ne II ORLs, along with their observed and dereddened intensities. We have determined extinction curves towards the 12 PNe using observed H I, He I and He II recombination line and continuum fluxes and radio free-free

continuum flux densities. Density and thermal characteristics of these PNe are studied using collisionally excited diagnostic lines and the H I recombination line and continuum spectrum. In a companion paper (Paper II) we present C, N, O, Ne, S, Cl and Ar abundances relative to hydrogen derived from UV, optical and IR CELs as well as heavy element abundances deduced from ORLs and we undertake an extensive comparison between the ORL and CEL elemental abundances. Differences between the ORL and the CEL abundances are then studied by searching for possible correlations between the ORL to CEL abundance ratio and other nebular properties. Finally, we discuss possible causes of the abundance and temperature determination discrepancies using the two types of emission line.

In Section 2 we describe the optical spectroscopic observations obtained with the William Herschel Telescope (WHT) 4.2-m telescope, the data reduction procedures, and present emission line fluxes. Line fluxes retrieved from *ISO* and *IUE* observations are also presented. Section 3 addresses interstellar extinction towards these nebulae. In Section 4 we present nebular electron temperatures and densities derived from heavy elemental CELs and from the Balmer discontinuity and high-order Balmer lines of the H I recombination spectrum.

## 2 OBSERVATIONS

Some basic data for the 12 sample nebulae are given in Table 1, including the observed flux of H $\alpha$  relative to H $\beta$ , the absolute total flux of H $\beta$ , the radio flux densities at 1.4 and 5.0 GHz and the nebular angular diameters measured in the optical and in the radio wavelengths.

### 2.1 Optical spectroscopy

The scanned, deep optical long-slit spectra of PNe analysed in the current work were obtained at the Observatorio del Roque de los Muchachos, La Palma, Spain, using the 4.2-m WHT, during two observing runs in 1996 August and 1997 August. An observational journal is presented in Table 2.

The ISIS long-slit double spectrograph was used in the two observing runs. For both the blue and red arms, a Tek 1024  $\times$  1024, 24  $\times$  24  $\mu\text{m}^2$  chip was used, which yielded a spatial sampling

along the slit of 0.3576 arcsec pixel $^{-1}$  projected on the sky. 600 and 316 groove mm $^{-1}$  gratings were used for the blue and red arms, respectively. All PNe were observed in four wavelength ranges, corresponding to two grating settings per spectral arm. For both observing runs, a 1-arcsec wide slit, oriented in the east–west direction (with a position angle of 90 $^\circ$ ), was used for nebular observations, with a resultant resolution of 1.5 and 3.5  $\text{\AA}$  FWHM for the blue and red spectra, respectively. Two *Hubble Space Telescope* (*HST*) spectrophotometric standard stars, BD+28 $^\circ$  4211 and HZ 44, were observed using a 6-arcsec wide slit for the purpose of flux calibration.

Exposure times ranged from 15 s to 20 min in order to obtain spectra covering a wide dynamical range. Integration times were carefully chosen such that strong emission lines would not be saturated in at least one short exposure, while long exposures were aimed at capturing an appropriate resolving power faint ORLs, whose intensities can be as low as a few times 10 $^{-4}$  that of H $\beta$ . In most cases, two or more frames were taken for exposures of long integration time in order to remove cosmic ray events and to reduce the noise level in the final combined spectrum.

During the two observing runs, each PN in our sample was scanned using a long slit across the nebular surface by uniformly driving the telescope differentially in right ascension. The observations thus yield average spectra for the entire nebula, which, when combined with the total H $\beta$  flux in the literature that was measured with a large entrance aperture (Table 1), yield absolute fluxes for all emission lines detected in our spectra. Optical line fluxes thus obtained are directly comparable to those in the UV and IR measured with space-borne facilities (such as the *IUE* and *ISO* satellites) which generally use a large entrance aperture that captures light from the whole nebula. A few nebulae in our sample have angular sizes larger than the *IUE* and *ISO* apertures. For these nebulae, some corrections must be applied to the UV and IR line fluxes to account for the effects of finite aperture sizes (see Sections 2.2 and 2.3).

Two-dimensional optical long-slit spectra were reduced using the LONG92 package in MIDAS. They were bias-subtracted, flat-fielded via division by a normalized flat-field, cleaned of cosmic rays, and then wavelength calibrated using exposures of a Th–Ar calibration lamp. Flux-calibration was achieved using wide-slit spectroscopic observations of *HST* standard stars. The latter step of data reduction was carried out using the IRAF software package.

**Table 1.** Basic data. The references cited are as follows: A92, Acker et al. (1992); AC79, Aller & Czyzak (1979); AC83, Aller & Czyzak (1983); AK87, Aller & Keyes (1987); B78, Barker (1978); CSC83, Carrasco, Serrano & Costero (1983); CK98, Condon & Kaplan (1998); CKS92, Cahn, Kaler & Stanghellini (1992); K83, Kaler (1983); O63, O’Dell (1963); P03, Pottasch et al. (2003a); P74, Perinotto (1974); PTP71, Peimbert & Torres-Peimbert (1971); ST01, Siódmiak & Tyłenda (2001); W42, Wyse (1942).

| PNG        | PN       | $F(\text{H}\alpha)$        | $-\text{Log}F(\text{H}\beta)$ (CKS92)   | $F(1.4 \text{ GHz})$ | $F(5 \text{ GHz})$ | Angular diameter (arcsec; A92) |         |
|------------|----------|----------------------------|---|----------------------|--------------------|--------------------------------|---------|
|            |          | $[F(\text{H}\beta) = 100]$ | ( $\text{erg cm}^{-2} \text{ s}^{-1}$ ) | (CK98) (mJy)         | (ST01) (mJy)       | (optical)                      | (radio) |
| 086.5–08.8 | Hu 1–2   | 430 (AC83) <sup>a</sup>    | 11.21 $\pm$ 0.01                        | 107.5                | 103.6(P03)         | 8.3                            | 1.7     |
| 123.6+34.5 | IC 3568  | 330 (B78)                  | 10.82 $\pm$ 0.01                        | 94.4                 | –                  | 10.0                           | –       |
| 120.0+09.8 | NGC 40   | 606 (AC79) <sup>a</sup>    | 10.37 (CSC83)                           | –                    | 470.0(CKS92)       | 48.0                           | –       |
| 043.1+37.7 | NGC 6210 | 301 (B78)                  | 10.09 $\pm$ 0.01                        | 298.0                | –                  | 16.2                           | –       |
| 034.6+11.8 | NGC 6572 | 380 (PTP71)                | 9.82 $\pm$ 0.02                         | 551.0                | 1260.0             | 10.8                           | 8.0     |
| 063.1+13.9 | NGC 6720 | 306 (B78)                  | 10.08 $\pm$ 0.03                        | 423.0                | 384.0(CKS92)       | 76.0                           | –       |
| 033.8–02.6 | NGC 6741 | 470 (W42)                  | 11.34 $\pm$ 0.01                        | 132.8                | 153.0              | 8.0                            | 6.0     |
| 041.8–02.9 | NGC 6781 | 598 (AK87) <sup>a</sup>    | 11.21 $\pm$ 0.04                        | 380.0                | 310.0              | 108.0                          | 130.0   |
| 037.8–06.3 | NGC 6790 | 540 (K83)                  | 10.90 $\pm$ 0.05                        | 53.1                 | 242.0              | 7.0                            | 1.8     |
| 083.5+12.7 | NGC 6826 | 288 (O63)                  | 9.96 $\pm$ 0.02                         | 415.0                | –                  | 25.0                           | –       |
| 082.1+07.0 | NGC 6884 | 551 (P74)                  | 11.11 $\pm$ 0.02                        | 152.8                | 175.2              | 6.0                            | 3.1     |
| 106.5–17.6 | NGC 7662 | 340 (O63)                  | 9.99 $\pm$ 0.01                         | 646.0                | 631.0              | 17.0                           | 26.0    |

<sup>a</sup>Calculated from the published dereddened intensity of H $\alpha$  using formula,  $F(\lambda) = 10^{-cf(\lambda)}I(\lambda)$ .

**Table 2.** Journal of the WHT observations.

| PN       | Date<br>(UT) | $\lambda$ range<br>(Å) | Exp. time<br>(s)                                    |
|----------|--------------|------------------------|---|
| Hu 1–2   | 97/08/09     | 3600–4400              | 20,206,600,700                                      |
|          |              | 4170–4970              | 20,44,456,861                                       |
|          |              | 5190–6670              | 20,38,452,856                                       |
|          |              | 6520–8010              | 20,200,654,700                                      |
| IC 3568  | 96/08/23     | 3590–4390              | 1000  |
|          |              | 4190–4990              | $2 \times 10,60,2 \times 1000$                      |
|          |              | 5280–6700              | $2 \times 10,60,1000$                               |
|          |              | 6599–7960              | 1000  |
| NGC 40   | 97/08/09     | 3600–4400              | 65,130,1200   |
|          |              | 4170–4970              | 38,65,1200  |
|          |              | 5190–6670              | 42,65,1200  |
|          |              | 6520–8010              | 65,130,1200   |
| NGC 6210 | 97/08/09     | 3600–4400              | $2 \times 20,532,538$                               |
|          |              | 4170–4970              | $2 \times 30,782,800$                               |
|          |              | 5190–6670              | $2 \times 30,777,802$                               |
|          |              | 6520–8010              | $2 \times 20,528,532$                               |
| NGC 6572 | 97/08/09     | 3600–4400              | $2 \times 15,3 \times 20,2 \times 100,2 \times 350$ |
|          |              | 4170–4970              | $2 \times 15,100,2 \times 110$                      |
|          |              | 5190–6670              | $2 \times 15,100,2 \times 110$                      |
|          |              | 6520–8010              | $2 \times 15,3 \times 20,2 \times 100,2 \times 350$ |
| NGC 6720 | 97/08/09     | 3600–4400              | 160,1200  |
|          |              | 4170–4970              | 50,160,1044,1200                                    |
|          |              | 5190–6670              | 50,160,1038,1200                                    |
|          |              | 6520–8010              | 160,2 $\times$ 1200                                 |
| NGC 6741 | 97/08/09     | 3600–4400              | 20,491,600  |
|          |              | 4170–4970              | 15,600  |
|          |              | 5190–6670              | 15,600  |
|          |              | 6520–8010              | 20,485,600  |
| NGC 6781 | 97/08/09     | 3600–4400              | 600   |
|          |              | 4170–4970              | 288,300   |
|          |              | 5190–6670              | 283,300   |
|          |              | 6520–8010              | 600   |
| NGC 6790 | 97/08/09     | 3600–4400              | $2 \times 15,464,600$                               |
|          |              | 4170–4970              | $2 \times 15,393,600$                               |
|          |              | 5190–6670              | $2 \times 15,388,600$                               |
|          |              | 6520–8010              | $2 \times 15,458,600$                               |
| NGC 6826 | 96/08/23     | 3590–4390              | $2 \times 22,2 \times 900$                          |
|          |              | 4190–4990              | $4 \times 22,2 \times 1200$                         |
|          |              | 5280–6700              | $4 \times 22,2 \times 1200$                         |
|          |              | 6599–7960              | $2 \times 22,2 \times 900$                          |
| NGC 6884 | 97/08/09     | 3600–4400              | 15,600  |
|          |              | 4170–4970              | 15,505,549  |
|          |              | 5190–6670              | 15,499,543  |
|          |              | 6520–8010              | 15,600  |
| NGC 7662 | 97/08/09     | 3600–4400              | $35,2 \times 900$                                   |
|          |              | 4170–4970              | $35,2 \times 900$                                   |
|          |              | 5190–6670              | $35,2 \times 900$                                   |
|          |              | 6520–8010              | $35,2 \times 900$                                   |

For each flux-calibrated two-dimensional spectrum, suitable sky windows were selected on both sides of nebular emission to generate the sky spectrum, which was then subtracted from the two-dimensional spectrum. The ISIS long slit had a useful length of over 4 arcmin, long enough to cover the whole nebula for all objects in our sample and leave enough clear area to sample the sky background. After sky-subtraction, the two-dimensional spectra were integrated along the slit direction over a length defined by nebular emission lines of interest to this work. For a few nebulae, their bright central stars significantly contaminated nearby nebular emission. In these cases, as appropriate, several spectral rows centred on the star were excluded from the integration.

Fig. 1 shows the optical spectrum of NGC 6210 from 3620 to 4820 Å after integration along the slit. Interstellar extinction has been corrected for using the extinction derived in Section 3. A synthetic spectrum, which includes recombination lines and continua of H I, He I and He II as well as emission lines produced by recombinations of doubly and triply ionized carbon, nitrogen, oxygen and neon ions, is overplotted in the figure, as a demonstration of the many recombination lines detected in the spectrum. Note also the weak Mg II  $\lambda 4481$  recombination line which has been clearly detected from this nebula.

All flux measurements were carried out on the sky-subtracted and extracted one-dimensional spectra. The results, normalized such that  $F(\text{H}\beta) = 100$ , are presented in Table 3. Fluxes of lines detected in blue-arm spectra were normalized using H $\beta$  fluxes measured from our own spectra. Fluxes of lines recorded in red-arm spectra were normalized using photometric H $\alpha$  fluxes relative to H $\beta$ , published in the literature and measured with a large entrance aperture and thus referred to the whole nebula (see Table 1). Several of the brightest lines were saturated in some deep spectra of long exposure time and their fluxes were retrieved from spectra of shorter integration time. Our measured line fluxes encompass a dynamic range of over  $10^4$ .

Fluxes of emission lines were measured using the MIDAS package using Gaussian line profile fitting techniques, except for the strongest ones for which fluxes obtained by simply integrating over the observed line profile were adopted. The results are tabulated in Table 3. Because PNe typically expand at velocities  $< 25 \text{ km s}^{-1}$  (e.g. Kwok 1994), much smaller than the instrumental broadening ( $\sim 92 \text{ km s}^{-1}$  for a FWHM of 1.5 Å at H $\beta$ , the best resolution of our optical spectra), it can be assumed that lines observed with a given instrumental setting all have the same linewidth as determined by the instrumental profile. Together with the accurately known laboratory wavelengths of detected lines, this reduces significantly the number of free (non-linear) parameters when fitting blended lines using multiple Gaussians. This procedure ensured accurate flux retrieval and aided line identification in cases where several lines blended together.

Given the large number of ORLs from abundant C, N, O and Ne ions and the fact that they are often quite weak and blended together, synthetic spectra were generated to aid line identifications and flux measurements. An example synthetic spectrum, which includes H I, He I and He II recombination lines, lines produced by recombinations of doubly and triply ionized C, N, O and Ne ions, as well as hydrogen and helium recombination continua, is shown in Fig. 1 and compared to the observed spectrum of NGC 6210. The synthetic spectrum also includes the Mg II 3d–4f  $\lambda 4481$  recombination line, the strongest of its type from a third-row element. The synthetic spectrum was convolved with a Gaussian profile to match the spectral resolution of the observation. The atomic data used to generate the synthetic spectrum are the same as described in Liu et al. (2000), except for the effective recombination coefficients of He I and N II lines for which the more recent calculations of Benjamin, Skillman & Smits (1999) and Kisielius & Storey (2002) were used, respectively. For the Mg II 3d–4f  $\lambda 4481$  line, we have assumed that it has an effective recombination coefficient equal to that of the C II 3d–4f  $\lambda 4267$  recombination line.

A synthetic spectrum calculated at a given nebular electron temperature and density yields relative strengths of ORLs arising from a given ion, which can be used to separate and retrieve fluxes of weak CELs blended with ORLs. A good example is the [S II] doublet  $\lambda\lambda 4068, 4076$  which falls in the wavelength region of the O II multiplet V10 ORLs (Fig. 2, upper panel). In this region the [S II]  $\lambda 4068$  line blends with two O II lines of multiplet V10, three C III

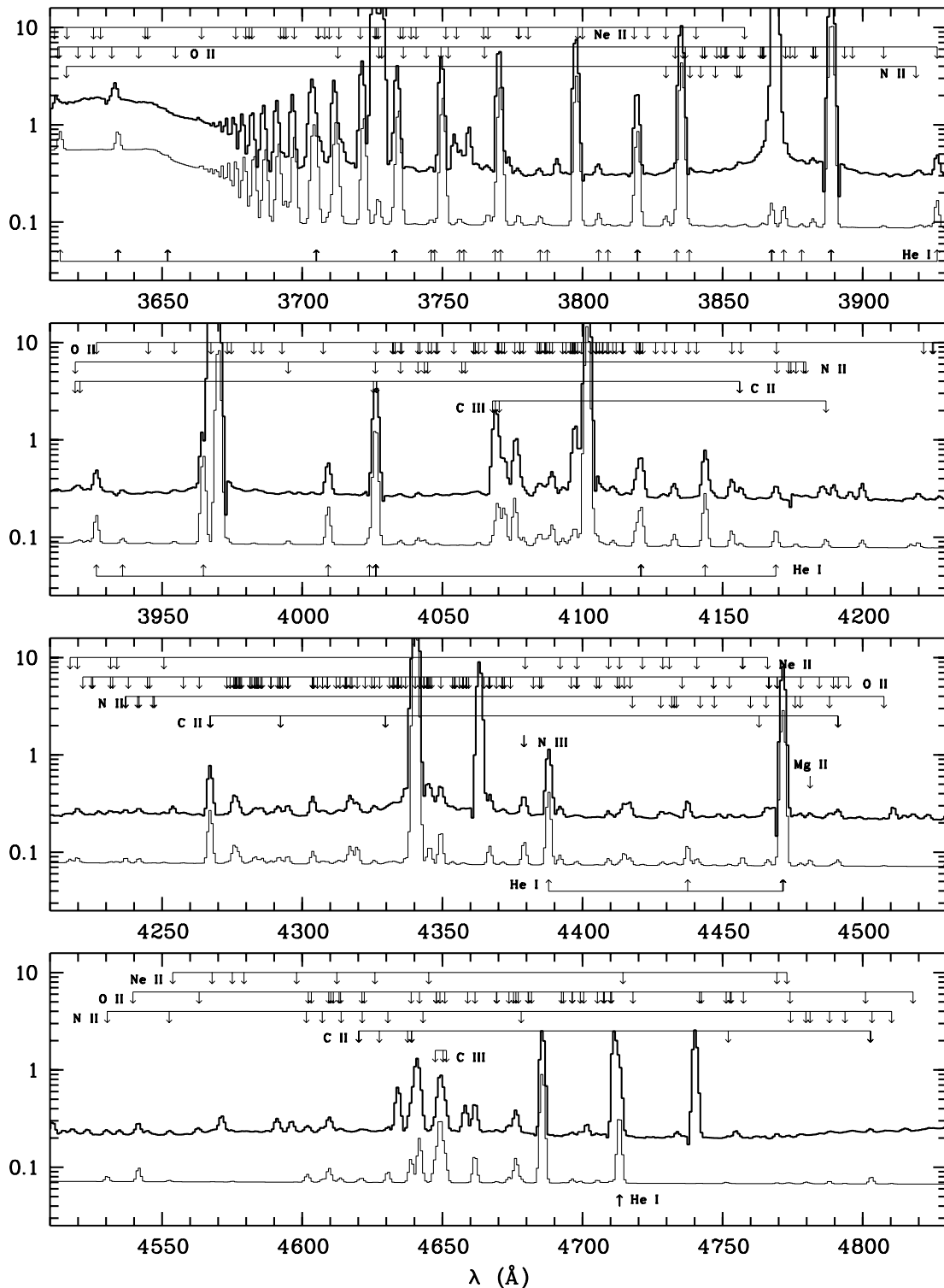


**Figure 1.** Optical spectrum of NGC 6210 (upper curve, scaled up by a factor of 3) from 3620 to 4820 Å. Also plotted is a synthetic spectrum (lower curve) which includes recombination continuum and line emission of H I, He I and He II as well as emission lines produced by recombinations of doubly and triply ionized carbon, nitrogen, oxygen and neon ions, as a demonstration of the rich ORL spectrum detected. Note also the weak Mg II  $3d-4f$  recombination line at 4481 Å. The spectrum has been corrected to laboratory wavelengths using H I Balmer lines and normalized such that  $I(H\beta) = 100$ . Interstellar extinction has been corrected for.

lines of multiplet V16 and the [S II]  $\lambda 4076$  line blends with another O II line of multiplet V10. However, the O II component of multiplet V10 at 4072 Å is reasonably clear from other lines. Because these O II lines arise from the same multiplet and their relative intensities

are essentially independent of the physical conditions in the nebula, the intensities of the O II blended with the [S II] forbidden lines can be estimated from observed intensity of the well-resolved O II component at 4072 Å. Similarly, the intensities of the three C III lines of

**Table 3.** Observed and dereddened line fluxes [ $F(\lambda)$  and  $I(\lambda)$ , respectively], on a scale where  $H\beta = 100$ . This is a sample of the full table, which is available on-line at <http://www.blackwellpublishing.com/products/journals/suppmat/MNR/MNR8155/MNR8155sm.htm>

| $\lambda_{\text{obs}}$ | Hu 1–2<br>$F(\lambda)$ | $I(\lambda)$ | Ion     | $\lambda_0$ | Mult |
|------------------------|------------------------|--------------|---------|-------------|------|
| 1240.36                | 16.960                 | 276.800      | N v     | 1238.82     |      |
| 1394.66                | 2.732                  | 25.440       | O iv]   | 1394.66     |      |
| 1403.80                | 11.930                 | 109.400      | O iv]   | 1403.06     |      |
| 1484.78                | 35.270                 | 284.800      | N iv]   | 1484.00     |      |
| 1549.28                | 98.080                 | 730.200      | C iv    | 1548.20     |      |
| 1640.57                | 95.560                 | 654.700      | He ii   | 1640.57     | 2.3  |
| 1664.98                | 9.860                  | 66.640       | O iii]  | 1664.98     |      |
| 1750.71                | 22.710                 | 151.300      | N iii]  | 1751.00     |      |
| 1884.17                | 3.957                  | 30.040       | Si iii] | 1883.00     |      |
| 1893.53                | 2.125                  | 16.430       | Si iii] | 1892.00     |      |
| 1906.54                | 19.570                 | 156.400      | C iii]  | 1906.54     |      |
| 1906.97                | 23.030                 | 184.100      | C iii]  | 1906.97     |      |
| 1908.58                | 12.980                 | 104.300      | C iii]  | 1908.58     |      |
| 1909.01                | 14.030                 | 112.700      | C iii]  | 1909.01     |      |

V16 can be estimated from intensities of other well-observed C III lines, such as the singlet at 4187 Å (multiplet V18) and the triplet near 4650 Å (multiplet V1). It is reasonable to assume that the three C III lines have relative intensities as given in *LS*-coupling. With all these constraints we find that it is possible to fit the O II and C III ORLs and the [S II] forbidden lines simultaneously and thus to retrieve the fluxes of the two [S II] lines fairly reliably, as indicated by their agreement with the theoretical  $\lambda 4068/\lambda 4076$  ratio of 3.08.

The spectral region near 4650 Å serves as another good example, where several lines from O II multiplet V1 blend with the three components of C III multiplet V1 (Fig. 2, lower panel). The spectral region from 4645 to 4680 Å was fitted by setting the relative intensities of the three C III lines to their corresponding values under *LS*-coupling.

In some cases several lines blended closely together and the data were not sufficient to yield unique fluxes for the individual components. For example, a broad asymmetric spectral feature at 4276 Å has been observed in many PNe, which is produced by over 10 lines blended together, all O II ORLs from the 3d–4f configuration (Fig. 2, middle panel). Although it is not possible to determine intensities of the individual components, an O II synthetic spectrum can be used to fit the data, yielding the total flux of the blend.

In general, except for the aforementioned cases, we have refrained from using a synthetic spectrum when measuring line fluxes, because in such cases the fluxes of individual components retrieved from the spectrum no longer yield independent information.

## 2.2 Infrared spectroscopy

11 PNe in our sample have been observed with the SWS and LWS on board *ISO*, yielding spectra from 2.4 to 45  $\mu\text{m}$  and 40–197  $\mu\text{m}$ , respectively. Fluxes of far-infrared (FIR) fine-structure lines from ionized regions, including the [O III] 52- and 88- $\mu\text{m}$ , [N II] 122- $\mu\text{m}$  and [N III] 57- $\mu\text{m}$  lines, for 10 PNe in our sample have been published by Liu et al. (2001a) who studied a large sample of 52 PNe using the LWS. They also obtained SWS spectra for many of the PNe in our sample. Line fluxes derived from these observations are included in the current analysis. They were measured on

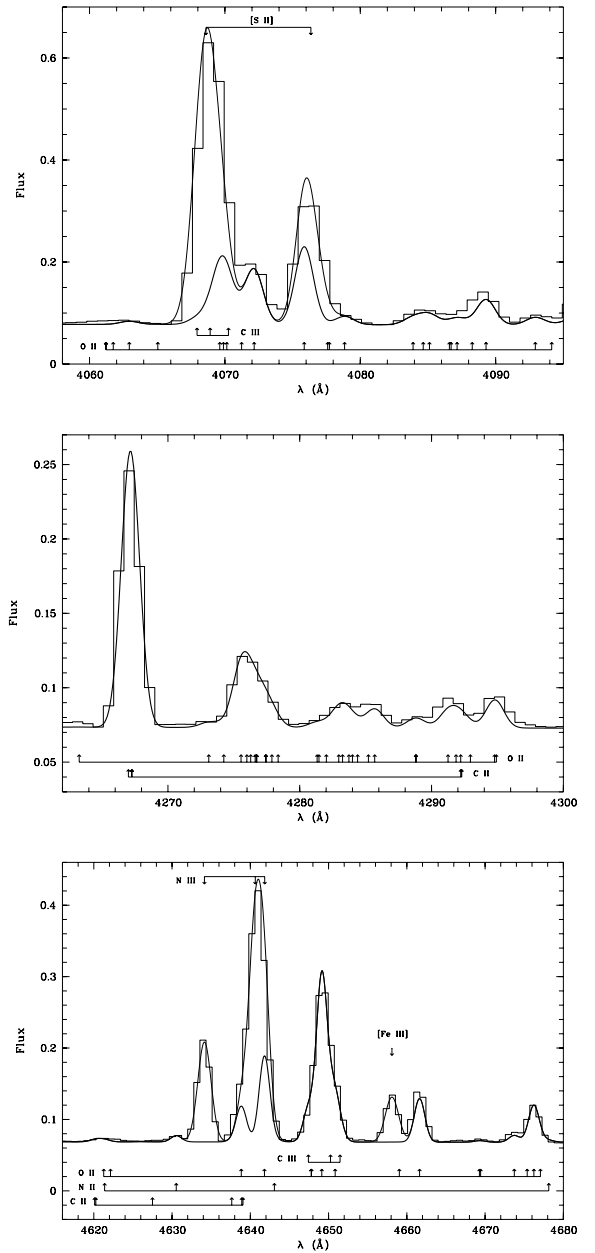


**Figure 2.** The optical spectrum of NGC 6210, showing selected wavelength regions in detail. The spectrum has a resolution of 1.5 Å FWHM. Upper panel: the  $\lambda\lambda 4058\text{--}4095$  region showing the blends of O II multiplet V10, C III V16 and the [S II] doublet. The blends were partially resolved and were fitted with multiple Gaussians with various constraints; see text for more details. The thick solid line is a synthetic spectrum showing the O II and C III recombination lines detected in the region, while the thin solid line represents the sum of all fitted Gaussians, including two for the [S II] doublet. Middle panel: the  $\lambda\lambda 4262\text{--}4300$  region showing the strong C III  $\lambda 4267$  ORL and a host of blended O II ORLs. The broad asymmetric feature near 4276 Å is a blend of over 10 O II ORLs, all originating from the 3d–4f configuration. The thick solid line is a synthetic spectrum including O II and C II recombination lines, which fits the observed spectrum very well. Lower panel: the  $\lambda\lambda 4616\text{--}4680$  region showing the blends of O II multiplet V1 and C III V1. The thick solid line is a synthetic spectrum of O II and C III recombination lines, and the thin solid line represents a simulated spectrum that includes all detected lines in the region, including the fluorescence-excited N III multiplet V2 and the [Fe III]  $\lambda 4658.10$  forbidden line.

**Table 4.** Merging factors. The references cited are as follows: P2003, Pottasch et al. (2003b); P2001, Pottasch et al. (2001).

| PN       | <i>IUE</i>   |  |  | <i>ISO</i> |            |              |              |
|----------|--|--|--|------------|------------|--------------|--------------|
|          | Method   | 1100–3300 Å  | Method   | 2.4–12 μm  | 12–29.5 μm | 29.5–45.2 μm | 43–197 μm    |
| NGC 40   | P2003  | –  | P2003  | 5.5        | 4.0        | 2.5          | –            |
| NGC 6210 | He II λ1640  | 1.00   |  |            |            |              |              |
| NGC 6720 | He II λ1640  | 12.67  | S <sub>PN</sub> /S <sub>aperture</sub><br>[Ne III] 15.5 μm<br>[S III] 33.5 μm    | 20.6       | 13.0       | 5.7          |              |
| NGC 6781 | –  | –  | S <sub>PN</sub> /S <sub>aperture</sub><br>S <sub>PN</sub> /S <sub>aperture</sub> | 51.4       | 38.1       | 21.8         | 1.14<br>2.94 |
| NGC 6826 | [N III] λ1750/57 μm<br>[O III] λ1665/λ4959<br>[O III] λ1665/(52 μm+88 μm)<br>Adopted | 4.148 ± 0.899<br>4.850 ± 0.003<br>5.301 ± 1.105<br>4.5 | H I 5.4/H γ  | 1.018      | 1.012      | 1.004        | –            |
| NGC 7662 | He II λ1640  | 1.96   | P2001  | 1.72       | 1.5        | 1.0          | –            |

spectra retrieved from the *ISO* Data Centre, Vilspa, Spain and processed with the SWS pipeline version 8.7. Pottasch et al. (2003b) presented SWS observations of NGC 40, Pottasch et al. (2001) presented SWS observations of NGC 6741 and 7662, and the *ISO* spectra of Hu 1–2 have been analysed by Pottasch et al. (2003a). We have adopted some of the SWS line fluxes published by these authors. Rubin et al. (1997) measured fluxes of two IR fine-structure lines for NGC 6210 using the *Kuiper Airborne Observatory (KAO)*. The measurements are also included in the current analysis.

The angular sizes of five PNe in our sample are larger than the SWS entrance aperture, which has a rectangle size of  $14 \times 20$  arcsec<sup>2</sup> for bands 1–2 (2.4–12 μm),  $14 \times 27$  arcsec<sup>2</sup> for bands 3A–3D (12.0–27.5 μm),  $20 \times 27$  arcsec<sup>2</sup> for band 3E (27.5–29.0 μm) and  $20 \times 33$  arcsec<sup>2</sup> for band 4 (29.0–45.2 μm). Two PNe in our sample, NGC 6720 and 6781, have an angular extension larger than even the LWS aperture, approximately 70 arcsec in diameter for wavelengths from 43–197 μm. For all these PNe of large angular size, the measured IR line fluxes were corrected for aperture effects using the correction factors listed in Table 4, estimated by comparing nebular angular extensions with the SWS and LWS aperture sizes.

IR fine-structure line fluxes after correction for aperture effects are listed in Table 3. They were normalized to  $F(\text{H}\beta) = 100$  using the total H $\beta$  fluxes listed in Table 1. Extinction corrections are discussed in Section 3.

### 2.3 *IUE* observations

We complement our optical and IR data set with *IUE* observations in the UV for 11 PNe; for NGC 6781, there are no available data from *IUE*. Low-resolution spectra obtained with the Short Wavelength Prime (SWP) and Long Wavelength Prime/Long Wavelength Redundant (LWP/LWR) cameras were retrieved from the *IUE* Newly Extracted Spectra (INES) Archive Data Server, Vilspa, Spain. For IC 3568, Hu 1–2, NGC 40 and 7662, high-resolution spectra are also available. SWP and LWP/LWR spectra cover the wavelength ranges of 1150–1975 and 1910–3300 Å, respectively. All the observations analysed were obtained with the *IUE* large aperture, a  $10.3 \times 23$  arcsec<sup>2</sup> oval and processed with the final (NEWSIPS) extraction method. When several spectra for a given nebula were available, they were co-added weighted by the integration times listed in Table 5. Fig. 3 shows the co-added SWP spectrum of NGC 6210 obtained with the large entrance aperture.

We measured the *IUE* emission line fluxes using the MIDAS package. The spectra were scrutinized and broad features and those show-

ing P Cygni profiles, indicating that they may originate from the stellar winds rather than the nebula, were discarded. For NGC 40, we use line fluxes adopted by Pottasch et al. (2003b). These measurements are reported by Clegg et al. (1983) and have been re-reduced by Feibelman (1999) using the NEWSIPS reduction program. For NGC 6741 and 7662, line fluxes were taken from Pottasch et al. (2001).

The angular sizes of five PNe are larger than the *IUE* aperture size (Table 1). For these nebulae, only a certain fraction of nebular UV emission was captured by the satellite. Procedures used to correct for this will be discussed in some detail in Section 2.4. The UV line fluxes were normalized to  $F(\text{H}\beta) = 100$  using the total H $\beta$  fluxes listed in Table 1, and then corrected for extinction using the reddening curves discussed in Section 3. For PNe with no detectable nebular He II λ1640 emission (NGC 40 and 6826), the amount of UV extinction towards them is quite uncertain. For these nebulae, the dereddened UV line fluxes given in Table 3 should be treated with caution.

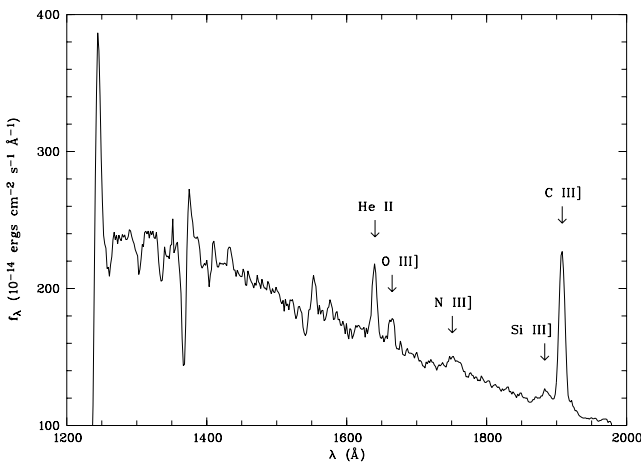
### 2.4 Spectral normalization

For the purpose of the current work, line fluxes measured with different instruments, both ground-based in the optical and space-borne in the UV and in the IR, have to be put on a common flux scale. In nebular analyses, it is common practice to scale all observed line intensities such that H $\beta$  has a flux of 100. For optical spectra covering the  $\lambda\lambda 4190\text{--}4990$  (or  $\lambda\lambda 4170\text{--}4970$ ) wavelength range taken with the ISIS blue arm, normalization was trivial as the spectra covered H $\beta$ . For spectra where H $\beta$  was saturated, as in the cases of some deep spectra of long integration time, a normalization factor was derived by comparing observed fluxes of (weaker) features, such as H $\gamma$  and He I λ4471 and He II λ4686, which were not saturated with those recorded on a spectrum of shorter exposure time where H $\beta$  was unsaturated. Blue-arm spectra spanning the  $\lambda\lambda 3590\text{--}4390$  (or  $\lambda\lambda 3600\text{--}4400$ ) wavelength range were brought to the same flux scale as those covering the  $\lambda\lambda 4190\text{--}4990$  (or  $\lambda\lambda 4170\text{--}4970$ ) range by comparing observed fluxes of lines covered by both wavelength settings, such as H $\gamma$  λ4340 and [O III] λ4363. Spectra taken with the ISIS red arm had no wavelength overlap with the blue-arm spectra and, as described earlier, the red-arm spectra were normalized using photometric measurements of H $\alpha$  relative to H $\beta$  for the whole nebula available in the literature.

For nebulae with angular sizes smaller than the *IUE* SWP/LWP and *ISO* SWS/LWS aperture, UV and IR line flux measurements were simply normalized using the total H $\beta$  fluxes listed in Table 1.

**Table 5.** Journal of *IUE* observations.

| PN       | Spectrum  | Dispersion | Exp. time (s)   |
|----------|---|------------|---|
| Hu 1–2   | SWP 13339,13945,42044,46578   | Low        | 2820,5400,1500,2400   |
|          | SWP 05431,07982,44662   | High       | 1200,10800,24300  |
|          | LWP 20788,24584   | Low        | 1800,1800   |
|          | LWR 06254   | Low        | 1800  |
| IC 3568  | SWP 14868   | High       | 23220   |
| NGC 40   | SWP 03076,09241,15412,15445,49087,49097,<br>49098,49635,49636,49638   | Low        | 900,6000,4200,10800,4200,6600<br>6000,9000,9000,4500                                  |
|          | SWP 49071   | High       | 16200   |
|          | LWP 26677,26695,26696,27076,27077   | Low        | 4860,7200,4500,6000,7200  |
|          | LWR 07999,11923,11924   | Low        | 1800,1200,7200  |
|          | SWP 13455,14650   | Low        | 1800,2100   |
| NGC 6210 | SWP 10733,16329,17925,47013,47014,47565,<br>54962,54963,54964,54965,54966,54967,<br>54968,54969,54970,54971 | Low        | 960,360,360,360,360,960,480<br>340,340,340,340,340,340,340<br>340,340,340,340         |
|          | LWP 24974   | Low        | 360   |
|          | LWR 10117,11241   | Low        | 4500,1500   |
|          | LWR 06782   | Low        | 420   |
|          | SWP 14652   | Low        | 240   |
| NGC 6572 | SWP 02485,02486,05716,10001,14917,47524   | Low        | 600,180,720,1500,360,1500   |
|          | LWR 11242   | Low        | 720   |
|          | LWP 25386   | Low        | 600   |
|          | LWR 02271,04945,07421   | Low        | 600,720,720   |
| NGC 6720 | SWP 06464,07219,07230,07231,07232,41639,<br>41640,41641,41642,41643,41647,41648<br>41649,41650,41651,41655  | Low        | 3600,3600,3600,5400,2400,4800<br>4080,1920,4200,5400,6000,2400<br>1800,3900,4800,6000 |
|          | LWP 20382,20383,20388,20389,20390,20393   | Low        | 7200,7200,7200,7200,6000,7200   |
|          | LWR 06238,06239,06240   | Low        | 5400,5400,2400  |
|          | SWP 05213   | Low        | 4200  |
| NGC 6741 | LWR 04508   | Low        | 3600  |
|          | SWP 06647,10000,10506,15411,15446,31831   | Low        | 1200,600,600,5400,2100,3600   |
| NGC 6790 | LWR 08709,11922,11935   | Low        | 1200,3600,1560  |
|          | SWP 14616,25254,25255   | Low        | 1200,600,480  |
| NGC 6826 | LWP 05376   | Low        | 480   |
|          | LWR 05430,11207,11215   | Low        | 1178,3600,3600  |
| NGC 6884 | SWP 17018   | Low        | 10800   |
| NGC 7662 | SWP 20097,20102,20105   | Low        | 3900,3600,7620  |
|          | LWR 11216,11239,11240   | Low        | 4500,2400,2100  |
|          | LWR 08000   | High       | 3420  |

**Figure 3.** Co-added *IUE* SWP spectrum of NGC 6210.

For the five nebulae whose angular sizes were larger than the *IUE* large aperture, flux measurements were corrected for aperture effects as described in Section 2.3 and then normalized using the total  $H\beta$  flux. The  $\text{He II } \lambda 1640$  line was well detected in NGC 6210, 6720 and 7662. UV line fluxes of these three nebulae were therefore normalized to  $H\beta$  by comparing the dereddened observed  $\text{He II } \lambda 1640/\lambda 4686$  ratio with that predicted by the recombination theory (Storey & Hummer 1995). For NGC 40, we have adopted fluxes published by Pottasch et al. (2003b), measured on spectra reprocessed with the new NEWSIPS reduction procedure by Feibelman (1999). The fluxes have been normalized to  $H\beta$  using two methods. In the first method, which was used by Clegg et al. (1983), the scaling factors were estimated by comparing the observed nebular continuum fluxes to those predicted by the recombination theory. The other way is by means of the  $[\text{O II}]$  line ratio  $I(\lambda 2470)/I(\lambda 7325) = 0.78$ . These lines arise from the same levels and therefore their intensity ratio is independent of the physical conditions in the nebula. In NGC 6826, the  $\text{N III] } \lambda 1750$  and  $\text{O III] } \lambda \lambda 1660, 1666$  lines have been detected by *IUE*. For this nebula, we normalized the UV line fluxes using

the predicted  $[\text{N III}] 57 \mu\text{m}/\lambda 1750$ ,  $[\text{O III}] \lambda 4959/(\lambda 1660 + \lambda 1666)$  and  $[\text{O III}] (52 \mu\text{m} + 88 \mu\text{m})/(\lambda 1660 + \lambda 1666)$  intensity ratios calculated with a multilevel atomic model for the adopted electron temperature and density for this nebula (see Section 4). The three line ratios yield an average merging factor of 4.5 for the UV lines.

IR data were obtained with a variety of aperture sizes. The *ISO* SWS aperture for wavelengths shorter than  $12 \mu\text{m}$  is comparable in size with the *IUE* aperture, and is slightly larger at longer wavelengths. Five nebulae in our sample have angular sizes bigger than the SWS aperture and thus need aperture corrections depending on wavelength. We estimated the correction factors based on the predicted intensity ratios of a variety of recombination lines and/or forbidden lines. For NGC 40, we have adopted the merging factors estimated by Pottasch et al. (2003b). For NGC 7662, we used the merging factors adopted by Pottasch et al. (2001). NGC 6720 and 6781 are bigger even than the *ISO* LWS aperture, which is about 70 arcsec in diameter. For these two nebulae, the merging factors were mainly estimated by comparing the nebular angular size to the aperture size. The adopted merging factors for *IUE* and *ISO* measurements are listed in Table 4 along with the methods used to obtain them.

Table 3 presents optical line fluxes for the 12 Galactic PNe in our sample, plus *IUE* line fluxes in the UV for 11 of them and IR fine-structure line intensities for 11 nebulae. Typical flux measurement uncertainties for optical lines are estimated to be less than 5 per cent for lines with an observed flux  $F(\lambda) \geq 0.2$  [in units where  $F(\text{H}\beta) = 100$ ], 10 per cent for those with  $0.1 \leq F(\lambda) \leq 0.2$ , 20 per cent for  $0.05 \leq F(\lambda) \leq 0.1$ , and 30 per cent or more for lines with  $F(\lambda) \leq 0.05$ .

It is interesting to note that the  $\text{He II } \lambda 4686$  line has been detected in the low-excitation nebula NGC 40, with an intensity of 0.044 in units where  $\text{H}\beta = 100$ . The line is narrow, with a FWHM of  $1.8 \text{ \AA}$ , typical for other nebular lines. NGC 40 has a WC8 central star. It is possible that the  $\lambda 4686$  feature reported in Table 3 is really just a narrow bump that is part of the stellar  $\lambda 4686$  feature (Wolf-Rayet stars often show multiple bumps in their line profiles). Alternatively, the detected  $\lambda 4686$  feature is indeed of nebular origin. Given that the 35 000–40 000 K central star of NGC 40 is unlikely to provide a significant number of photons that can ionize nebular  $\text{He}^+$  ions, one possibility might be that  $\text{He}^{2+}$  is ionized in shock fronts where the stellar wind impacts nebular material.

### 3 EXTINCTION

Before proceeding to nebular plasma diagnostic analyses, measured line fluxes need to be corrected for the effects of dust extinction. Extinction towards PNe is generally dominated by interstellar dust grains, although it is known that some PNe, such as NGC 7027 and 6302 are surrounded by dusty neutral and molecular envelopes (Seaton 1979; Lester & Dinerstein 1984; Middlemass 1990). It is usually assumed that for Galactic disc PNe, the standard Galactic extinction law for the diffuse interstellar medium (ISM) with a total-to-selective extinction ratio,  $R \equiv A(V)/E_{B-V} = A(V)/[A(B) - A(V)] = 3.1$  (e.g. Howarth 1983), applies, and the amount of extinction can be characterized by a single parameter, the logarithmic extinction at  $\text{H}\beta$ ,  $c(\text{H}\beta)$ . However, it is also known that dust extinction curves may vary significantly along different sight lines, especially in the UV, and that the extinction and scattering properties of dust grains exposed to intense UV radiation fields, such as those encountered near  $\text{H II}$  regions and in circumstellar envelopes, can be different from those of dust grains found in the general diffuse ISM (Cardelli, Clayton & Mathis 1989). For example, it has

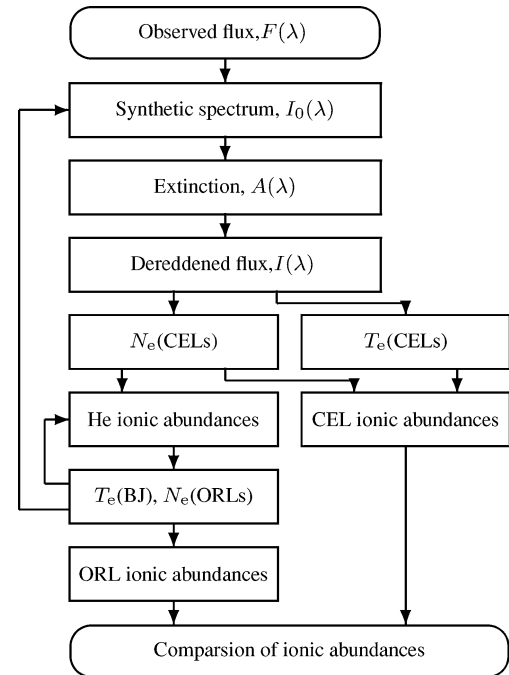


Figure 4. Flow chart of nebular analysis.

been found that the far-UV extinction curve towards the Galactic Centre is much steeper than the standard extinction law for Galactic diffuse medium (Walton, Barlow & Clegg 1993; Liu et al. 2001b), and the extinction towards the B3 V star HD 210121, obscured by the high-latitude cloud DBB 80, yields  $R = 2.1 \pm 0.2$ , rather than the standard value of  $R = 3.1$  for the general ISM (Welty & Fowler 1992; Larson, Whittet & Hough 1996). The multiwavelength observations from the UV to the FIR that we have accumulated for PNe in our sample, combined with the radio continuum measurements (see Table 1), allow us not only to derive the amount of reddening towards the PN,  $c(\text{H}\beta)$ , but also in some cases enable us to determine the shape of the extinction curve along the sight line.

The emissivities of recombination lines and continua of  $\text{H I}$ ,  $\text{He I}$  and  $\text{He II}$ , as well as the bremsstrahlung radio continuum emission, have only a weak, similar, power-law dependence on electron temperature and essentially none on electron density. Thus, dust extinction towards a given nebula can be determined by comparing with theoretical predictions the observed fluxes of the  $\text{H I}$  recombination continuum and lines relative to the radio continuum flux density. To account for the weak dependence on electron temperature, density and helium ionic abundances of the ratio of the UV and optical  $\text{H I}$  recombination spectrum to the radio continuum flux density, some iterations are needed. Fig. 4 is a chart illustrating the flow of our plasma diagnostic and abundance analysis, including reddening corrections.

First, a preliminary extinction and plasma diagnostic analysis was carried out, using the standard Galactic extinction law of Howarth (1983) assuming a total-to-selective extinction ratio  $R = 3.1$ . Helium ionic abundance ratios,  $y^+ \equiv \text{He}^+/\text{H}^+$  and  $y^{++} \equiv \text{He}^{++}/\text{H}^+$ , were calculated from the dereddened fluxes of observed  $\text{He I}$  and  $\text{He II}$  recombination lines. The preliminary electron temperature, density and helium ionic abundance ratios were then used to calculate a theoretical synthetic  $\text{H I}$ ,  $\text{He I}$  and  $\text{He II}$  recombination spectrum (including contributions from lines and continua). The synthetic spectrum

was then compared with the observation to determine the optical and UV extinction curve towards the nebula. The process was repeated (one iteration was usually sufficient in most cases) until the estimates for extinction, electron temperature and density as well as helium ionic abundances all converged.

Let  $F(\lambda)$  and  $I(\lambda)$  denote the observed and intrinsic line flux (or continuum flux density per Å), respectively, then

$$I(\lambda) = 10^{c(\text{H}\beta)[1+f(\lambda)]} F(\lambda),$$

where  $f(\lambda)$  is the extinction curve normalized such that  $f(\text{H}\beta) = 0$ . The extinction in magnitudes at a given wavelength  $\lambda$  is given by

$$A(\lambda) = 2.5c(\text{H}\beta)[1 + f(\lambda)].$$

Given the nebular electron temperature and density and helium ionic abundance ratios, the intrinsic intensity  $I(\lambda)$  of a hydrogen recombination line, e.g.  $\text{H}\beta$ , can be calculated from the radio free-free continuum flux density measured at a given frequency  $\nu$ , for example 5 GHz, assuming that the nebula is optically thin at this frequency (Milne & Aller 1975). By comparing the observed flux of a  $\text{H I}$  recombination line (Balmer series only in our case) with that predicted by the radio continuum flux density, the extinction  $A(\lambda)$  at the wavelength of the  $\text{H I}$  recombination line can be determined.

Similarly, by comparing the observed flux ratio of two  $\text{He I}$  or  $\text{He II}$  recombination lines at wavelengths  $\lambda_1$  and  $\lambda_2$ , respectively, with the theoretical value predicted by recombination theory, the magnitude of the differential extinction between these two wavelengths can be determined. For example, from the observed  $\text{He II } F(\lambda 1640)/F(\lambda 4686)$  line ratio, the value of  $A(\lambda 1640) - A(\lambda 4686)$  can be determined.  $A(\lambda 4686)$  can be obtained by interpolating  $A(\lambda 4340)$  and  $A(\lambda 4861)$ , after the latter two values have been determined from the observed fluxes of  $\text{H}\gamma$  and  $\text{H}\beta$ , respectively. In this way,  $A(\lambda 1640)$  can be determined.

The nebular continuum Balmer discontinuity at 3645 Å can be treated as a recombination ‘line’. The ratio of the Balmer jump to  $\text{H 11}$  at 3770 Å, which is insensitive to reddening corrections, has been used to derive nebular electron temperatures (e.g. Liu et al. 2001b). By comparing the observed ratio of the Balmer jump to  $\text{H}\beta$  with the value calculated from recombination theory, using the electron temperature derived from the Balmer jump to  $\text{H 11}$  ratio, the extinction at 3645 Å can be determined.

The method outlined above for determining  $A(\lambda)$  [or equivalently  $f(\lambda)$ ] using hydrogen and helium recombination lines can be extended to nebular continuum emission, as the latter is also produced by recombinations of ionized hydrogen and helium with electrons, except that in this case the emission is produced by free-bound transitions and two-photon emission of the  $\text{H I } 2s^2\text{S}$  metastable level. By comparing the observed and predicted flux densities of nebular continuum emission as a function of wavelength, a complete extinction curve  $A(\lambda)$  can be determined. Groves et al. (2002) used this method to obtain an extinction curve for the internal dust of NGC 6302. Much earlier, Grewing et al. (1978) and Seaton (1979) used the hydrogen and helium recombination line spectra to study the interstellar and circumstellar dust extinction towards the bright young compact PN NGC 7027. Greenstein (1981) has found anomalous extinction properties for the circumstellar dust grains in the old PN Abell 30 that share many similarities to the laboratory measurements of carbon smoke (see also Harrington 1996). The continuum analysis is however complicated by the fact that the observed continuum can be contaminated by starlight from the central star. To account for this, in our analysis, we have included in our synthetic spectrum a blackbody to simulate the direct/scattered stellar light,

$I_s(\lambda) \propto B(\lambda)$ , assuming a constant effective temperature of  $T_{\text{eff}} = 50\,000$  K for the central stars of all PNe.

The extinction curves thus derived towards sight lines of PNe in our sample are presented in Fig. 5 for IC 3568, Hu 1–2, NGC 6210 and 6572. The radio continuum flux densities and total  $\text{H}\beta$  fluxes used in the analyses are listed in Table 1. Electron temperatures and densities adopted in the analysis were based on results derived from a variety of CEL and ORL diagnostic ratios (see Section 4, Table 7). For self-consistency,  $T_e(\text{BJ})$  derived from the  $\text{H I}$  Balmer jump was used for all PNe except for the low surface brightness nebula NGC 6781, for which our data were too noisy to yield a meaningful measurement of the Balmer jump temperature. For this nebula, we have adopted the electron temperature derived from the  $[\text{O III}]$  optical forbidden-line ratio,  $T_e(\text{O III})$ . For the electron density, we have used the average values deduced from a variety of optical forbidden-line diagnostic ratios,  $N_e(\text{CEL})$ . As we shall see in Section 4.2.2, electron densities deduced from high-order Balmer lines are generally consistent with those derived from forbidden-line ratios. Helium ionic abundance ratios,  $\text{He}^+/\text{H}^+$  and  $\text{He}^{++}/\text{H}^+$ , adopted in the analyses will be presented in Paper II. They were derived assuming  $T_e(\text{BJ})$  and  $N_e(\text{CEL})$  for the electron temperature and density, respectively.

We use the  $R$ -dependent Galactic extinction law of Cardelli et al. (1989) to fit the extinction data derived from various methods by varying  $R$ . For most objects, we find that the standard Galactic extinction law of  $R = 3.1$  for diffuse ISM gives an adequate fit to the data (e.g. IC 3568 in Fig. 5). There are however notable exceptions. We find that the UV extinction towards Hu 1–2 is much steeper than for the general ISM and the data are best fitted with a low value of  $R = 2.0$ . Values of extinction  $A(\lambda)$  towards Hu 1–2 derived from various  $\text{H I}$ ,  $\text{He I}$  and  $\text{He II}$  lines are listed in Table 6. For  $R = 2.0$ , we find that the data yield a logarithmic extinction at  $\text{H}\beta$ ,  $c = 0.51$ . Fig. 6 shows a segment of the observed blue-arm spectrum of Hu 1–2 around the Balmer jump region. Two synthetic spectra, reddened with  $c(\text{H}\beta) = 0.51$  and assuming, respectively,  $R = 2.0$  (thin solid line) and  $R = 3.1$  (dashed line), are also overplotted and compared to the observation. Fig. 6 clearly shows that the extinction law of  $R = 2.0$  gives a much better fit to the data, both for the  $\text{H I}$  Balmer decrement and the Balmer jump. [Note that  $T_e(\text{BJ})$ , derived from the ratio of the Balmer jump at 3646 Å to  $\text{H 11}$  at 3770 Å, is nearly independent of the extinction corrections.] In their recent analysis of Hu 1–2, Pottasch et al. (2003a) used the standard  $R = 3.1$  Galactic extinction law for the diffuse ISM and adopted  $c = 0.60$ . They noted that the  $\text{He II } \lambda 1640/\lambda 4686$  ratio yields a higher reddening constant of 0.74, whereas the  $\text{IR Br}\alpha$  line gives a lower value of  $c = 0.44$ . Note that Hu 1–2, as well as NGC 6572 discussed below, are all compact nebulae. Sabbadin, Cappellaro & Turatto (1987) have obtained deep images of Hu 1–2 in  $\text{H}\alpha$ , which show that the nebula has an angular size of approximately  $12 \times 8$  arcsec<sup>2</sup> down to 5 per cent of peak intensity level, although emission at very low levels has been detected out to a radius of 10–12 arcsec. Therefore, the *IUE* large aperture should have captured essentially all UV emission from this nebula and the steep rise of extinction in the UV observed towards Hu 1–2 is unlikely to be caused by calibration problems when comparing the optical and UV data. We will adopt an extinction curve with  $R = 2.0$  in our further analysis of this nebula.

There is some evidence that the UV extinction towards the young and compact bright PN NGC 6572 is also steeper than for the general ISM. However, the optical and IR extinction towards this nebula is well described by the standard reddening law with  $R = 3.1$ . Thus, for NGC 6572, we have adopted the standard reddening law. However, in order to minimize systematic errors of UV line fluxes, all UV lines

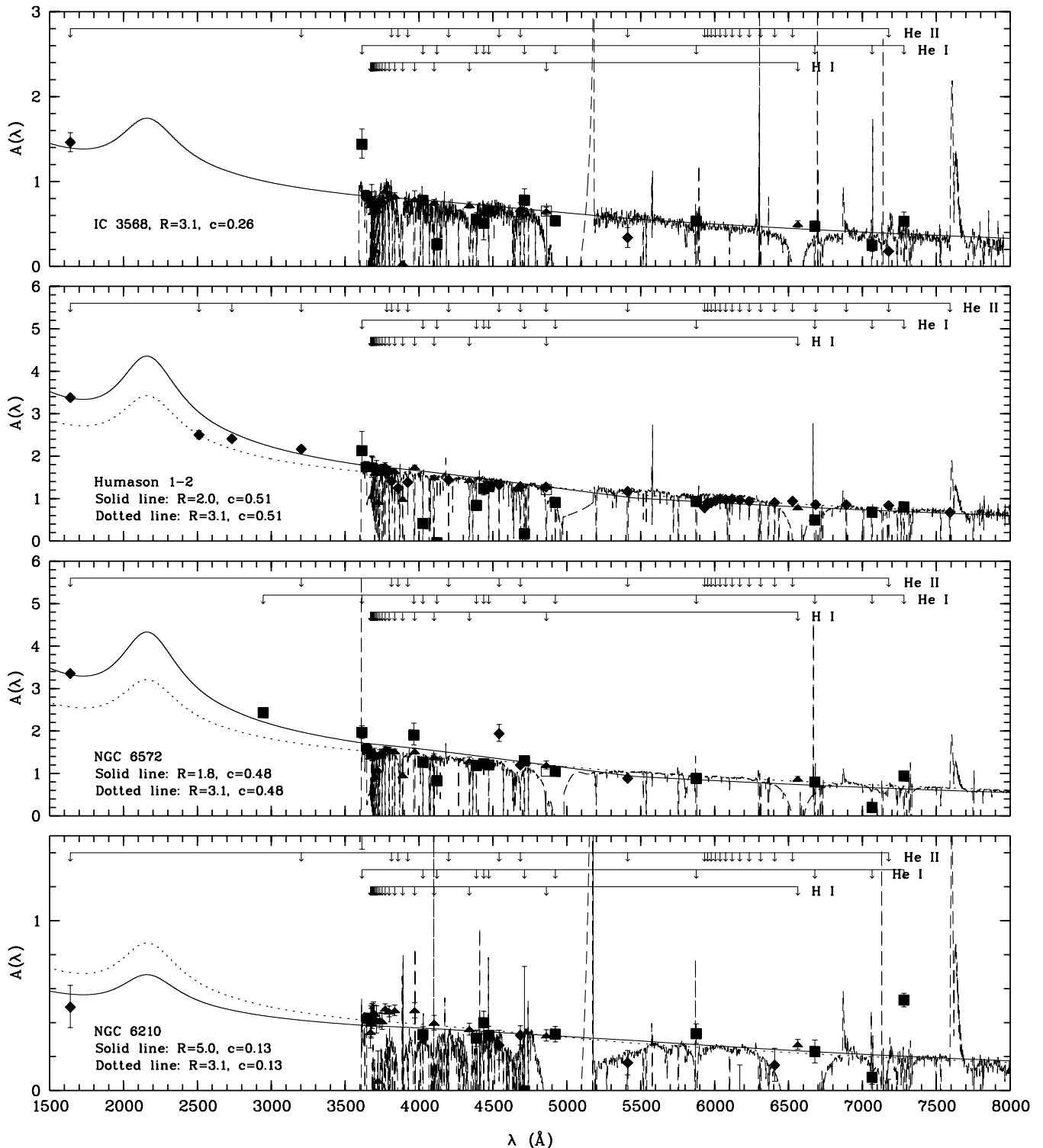


**Figure 5.** Extinction as a function of wavelength for four PNe in our sample. Symbols denote values derived from H I (triangles), He I (squares) and He II (diamonds) recombination lines, as well as from the H I recombination continuum Balmer discontinuity. The dashed lines represent extinction curves derived from the nebular continuum spectra. In each panel, the standard  $R$ -dependent reddening law of Cardelli et al. (1989) that best fits the data is shown as a solid line. In some panels, a comparison curve with a different value of  $R$  is also shown as a dotted line. The prominent dip and peak near 5000  $\text{\AA}$  are artefacts in the observed spectra caused by scattered light of the strong [O III]  $\lambda 5007$  line, which fell just outside the spectral wavelength coverage of both our blue spectra ( $\lambda < 4990$   $\text{\AA}$ ) and red spectra ( $\lambda > 5280$   $\text{\AA}$ ).

were dereddened relative to the He II  $\lambda 1640$  line and then scaled such that the He II  $\lambda 1640/\lambda 4686$  line ratio after reddening corrections agrees with its theoretical value predicted by the recombination theory.

Contrary to the cases of Hu 1–2 and NGC 6572, the UV extinction towards NGC 6210 is found to be somewhat shallower than for the general ISM. The total extinction towards this nebula is relatively small,  $c = 0.13$ , so the uncertainties in our reddening estimates can

**Table 6.** Extinction towards Humason 1–2.

| ID                | $\lambda$<br>(Å) | $1/\lambda$<br>( $\mu\text{m}^{-1}$ ) | $A(\lambda)$<br>(mag) |
|-------------------|------------------|---------------------------------------|-----------------------|
| He II             | 7592.74          | 1.317                                 | 0.58                  |
| He I              | 7281.35          | 1.373                                 | 0.47                  |
| He II             | 7177.50          | 1.393                                 | 0.50                  |
| He I              | 7065.25          | 1.415                                 | 0.65                  |
| He II             | 6890.88          | 1.451                                 | 0.55                  |
| He II             | 6683.20          | 1.496                                 | 0.60                  |
| He I              | 6678.16          | 1.497                                 | 1.00                  |
| H 3, He II        | 6562.77          | 1.524                                 | 0.82                  |
| He II             | 6527.11          | 1.532                                 | 0.53                  |
| He II             | 6406.30          | 1.561                                 | 0.62                  |
| He II             | 6233.80          | 1.604                                 | 0.63                  |
| He II             | 6170.60          | 1.621                                 | 0.60                  |
| He II             | 6118.20          | 1.634                                 | 0.57                  |
| He II             | 6074.10          | 1.646                                 | 0.62                  |
| He II             | 6036.70          | 1.657                                 | 0.60                  |
| He II             | 6004.73          | 1.665                                 | 0.71                  |
| He II             | 5977.03          | 1.673                                 | 0.81                  |
| He II             | 5952.94          | 1.680                                 | 0.81                  |
| He II             | 5931.84          | 1.686                                 | 1.10                  |
| He I              | 5875.66          | 1.702                                 | 0.69                  |
| H $\beta$ , He II | 4861.33          | 2.057                                 | 0.94                  |
| He II             | 4541.59          | 2.202                                 | 0.69                  |
| H 5               | 4340.47          | 2.304                                 | 1.02                  |
| He II             | 4199.83          | 2.381                                 | 1.04                  |
| H 6               | 4101.74          | 2.438                                 | 1.08                  |
| H 7               | 3970.07          | 2.519                                 | 2.00                  |
| H 9               | 3835.39          | 2.607                                 | 1.45                  |
| H 10              | 3797.90          | 2.633                                 | 1.62                  |
| He II             | 3781.72          | 2.644                                 | 1.37                  |
| H 11              | 3770.63          | 2.652                                 | 1.91                  |
| H 12              | 3750.15          | 2.667                                 | 1.75                  |
| H 13              | 3734.37          | 2.678                                 | 1.49                  |
| H 15              | 3711.97          | 2.694                                 | 1.81                  |
| H 16              | 3703.86          | 2.700                                 | 1.19                  |
| H 17              | 3697.15          | 2.705                                 | 1.56                  |
| H 18              | 3691.56          | 2.709                                 | 1.55                  |
| H 19              | 3686.83          | 2.712                                 | 1.86                  |
| H 20              | 3682.81          | 2.715                                 | 1.75                  |
| H 21              | 3679.36          | 2.718                                 | 1.63                  |
| H 22              | 3676.36          | 2.720                                 | 1.67                  |
| H 23              | 3673.74          | 2.722                                 | 1.79                  |
| H 24              | 3671.48          | 2.724                                 | 1.76                  |
| BJ                | 3646.00          | 2.743                                 | 1.72                  |
| He II             | 3203.10          | 3.122                                 | 2.55                  |
| He II             | 2733.30          | 3.659                                 | 2.35                  |
| He II             | 2510.58          | 3.983                                 | 2.18                  |
| He II             | 1640.57          | 6.095                                 | 3.47                  |

be significant. Thus, as in the case of NGC 6572, we have adopted the standard reddening law of  $R = 3.1$  but dereddened the UV line fluxes relative to the He II  $\lambda 1640$  line.

For all other nebulae in our sample, we have used the standard Galactic reddening law with  $R = 3.1$ . The adopted extinction constants for individual nebulae are listed in Table 7.

## 4 PLASMA DIAGNOSTICS

### 4.1 Collisionally excited lines

Nebular electron temperatures  $T_e$  and densities  $N_e$  have been derived from a variety of CEL diagnostic ratios by solving level populations

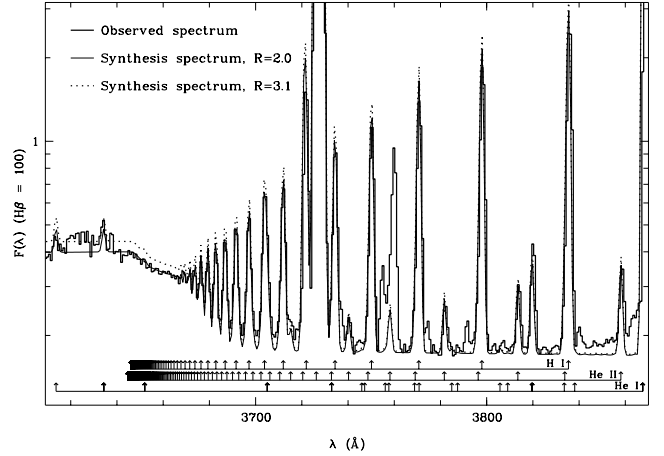


**Figure 6.** The observed blue spectrum of Hu 1–2 from 3610 to 3870 Å (thick solid line), showing the nebular continuum Balmer discontinuity at 3646 Å. The ratio of the Balmer jump to H 11  $\lambda 3770$  yields an electron temperature of 18 900 K, just 600 K lower than the value derived from the [O III] nebular auroral line ratio. Two synthetic spectra are overplotted, reddened for a logarithmic extinction at H $\beta$  of  $c(\text{H}\beta) = 0.51$  and assuming, respectively,  $R = 3.1$  (dashed line) and  $R = 2.0$  (thin solid line). All spectra were normalized such that  $F(\text{H}\beta) = 100$ . The continuum level of the two synthetic spectra at 3700 Å have been shifted to match the observation.

for a multilevel ( $\geq 5$ ) atomic model using EQUIB, a FORTRAN program originally written by I. D. Howarth and S. Adams. The results are presented in Table 7. Columns 1–3 give, respectively, the diagnostic ratio identification number, diagnostic ratio and ionization potential required to produce the ion emitting the diagnostic lines. The first part of Table 7 lists temperature diagnostic ratios and temperatures derived from these ratios. Density-diagnostic ratios and the resultant densities are given in the second part. The atomic data used to derive the results and throughout this work are the same as those summarized by Liu et al. (2000) in their case study of the PN NGC 6153. Diagnostic diagrams for 12 nebulae, which plot the loci of various diagnostic line ratios in the  $T_e - \log N_e$  plane, are presented in Fig. 7.

In all, 13 forbidden-line diagnostic ratios have been used to determine electron temperatures and nine have been used for densities, although not all diagnostics are available for each PN. The transauroral line to nebular line ratio [O II] ( $\lambda 7320 + \lambda 7330$ )/( $\lambda 3726 + \lambda 3729$ ) is sensitive to both  $T_e$  and  $N_e$  and the temperatures listed in Table 7 were derived assuming an electron density as deduced from the [O II] nebular line ratio ( $\lambda 3729/\lambda 3726$ ). Similarly, electron temperatures derived from the [O III] FIR fine-structure line to optical nebular line ratio ( $52 \mu\text{m} + 88 \mu\text{m}$ )/ $\lambda 4959$  were calculated assuming the electron density yielded by the density-sensitive FIR line ratio  $88 \mu\text{m}/52 \mu\text{m}$ . The temperature and density-diagnostic lines analysed here arise from a variety of ions with ionization potentials ranging from 10.4 eV (S II) to 63.5 eV (Ne V). It is expected that ions with similar ionization potentials form in similar ionization zones. We have therefore grouped various diagnostics based on ionization potential and paired the temperature- and density-diagnostic ratios accordingly. The density derived from a density-sensitive diagnostic ratio (e.g. [S II]  $\lambda 6731/\lambda 6716$ ) was normally calculated assuming an electron temperature derived from a temperature-sensitive diagnostic ratio of comparable ionization potential (e.g. from [N II] ( $\lambda 6548 + \lambda 6584$ )/ $\lambda 5754$ )). A similar philosophy was adopted when determining electron temperatures. In this way, for each nebula we

**Table 7.** Extinction and plasma diagnostics.

| ID | Diagnostic ratio  | I.P. (eV) | Hu 1–2                        | IC 3568         | NGC 40                            | NGC 6210               | NGC 6572                          |                         |                 |
|----|---|-----------|-------------------------------|-----------------|-----------------------------------|------------------------|-----------------------------------|-------------------------|-----------------|
|    |   |           |                               |                 | Ratio/ $T_e(10^3 \text{ K})$      |                        |                                   |                         |                 |
| 1  | [S II] na $(\lambda 6716 + \lambda 6731)/(\lambda 4068 + \lambda 4076)$ | 10.4      | 2.39/15.6                     |                 | 9.02/7.35                         | 2.81/12.6              | 0.956/8.70                        |                         |                 |
| 2  | [O II] na $(\lambda 3726 + \lambda 3729)/(\lambda 7320 + \lambda 7330)$ | 13.6      | 6.77/15.6                     | 9.97/16.6       | 34.9/8.68                         | 8.20/13.2              | 3.06/ <sup>d</sup>                |                         |                 |
| 3  | [N II] na $(\lambda 6548 + \lambda 6584)/\lambda 5754$                  | 14.5      | 45.4/13.0                     | 29.2/17.8       | 139./8.38                         | 63.2/11.1              | 37.8/13.6                         |                         |                 |
| 4  | [S III] fa $18.7\mu\text{m}/\lambda 6312$                               | 23.3      |                               | 17.8/10.5       | 44.3/8.33                         |                        |                                   |                         |                 |
| 5  | [Ar III] fn $9.0\mu\text{m}/(\lambda 7135 + \lambda 7751)$              | 27.6      |                               |                 | 1.16/7.89                         |                        |                                   |                         |                 |
| 6  | [Ar III] na $(\lambda 7135 + \lambda 7751)/\lambda 5192$                |           | 68.5/15.6                     | 171./10.4       |                                   | 263./8.93              | 169./10.4                         |                         |                 |
| 7  | [O III] na $\lambda 4959/\lambda 4363$                                  | 35.1      | 10.5/19.5                     | 35.6/11.4       | 44.5/10.6                         | 59.5/9.68              | 43.0/10.6                         |                         |                 |
| 8  | [O III] fa $\lambda 4959/(88 \mu\text{m} + 52 \mu\text{m})$             |           | 14.5/ $\gtrsim 20.0^a$        | 1.70/12.9       | 1.07/10.5                         | 8.22/8.38 <sup>a</sup> | 10.8/18.0                         |                         |                 |
| 9  | [Ne III] fa $15.5\mu\text{m}/\lambda 3868$                              | 41.0      | 0.346/17.2                    | 1.54/10.0       | 1.40/10.4                         |                        |                                   |                         |                 |
| 10 | [O IV] fu $25.9\mu\text{m}/\lambda 1400$                                | 54.9      | 2.03/20.8                     |                 |                                   |                        |                                   |                         |                 |
| 11 | [Ne IV] nu $\lambda 2425/\lambda 4725$                                  | 63.5      | 85.3/19.5                     |                 |                                   |                        |                                   |                         |                 |
| 12 | [Ne V] fu $\lambda 3425/24.3\mu\text{m}$                                | 97.1      | 1.23/21.0                     |                 |                                   |                        |                                   |                         |                 |
| 13 | [Mg V] fu $\lambda 2783/5.61\mu\text{m}$                                | 109.      | 1.21/18.3                     |                 |                                   |                        |                                   |                         |                 |
| 14 | Balmer jump   |           | /18.9                         | /9.49           | /7.02                             | /9.30                  | /11.0                             |                         |                 |
|    |   |           |                               |                 | Ratio/ $\log N_e(\text{cm}^{-3})$ |                        |                                   |                         |                 |
| 1  | [S II] nn $\lambda 6731/\lambda 6716$                                   | 10.4      | 1.67/3.69                     | 1.29/3.28       | 1.37/3.24                         | 1.66/3.64              | 2.11/4.41                         |                         |                 |
| 2  | [O II] nn $\lambda 3726/\lambda 3729$                                   | 13.6      | 2.06/3.69                     | 1.56/3.40       | 1.35/3.12                         | 1.99/3.65              | 2.48/4.02                         |                         |                 |
| 3  | [S III] ff $33.4\mu\text{m}/18.7\mu\text{m}$                            | 23.3      |                               |                 | 0.603/3.22                        |                        | 1.25/2.54                         |                         |                 |
| 4  | [Cl III] nn $\lambda 5537/\lambda 5517$                                 | 23.8      | 1.27/3.63                     |                 | 0.839/2.94                        | 1.17/3.49              | 2.27/4.18                         |                         |                 |
| 5  | C III] uu $\lambda 1909/\lambda 1907$                                   | 24.4      | 0.699/3.54                    | 0.818/3.91      | 0.850/4.00                        |                        |                                   |                         |                 |
| 6  | N III] uu $\lambda 1752/\lambda 1749.7$                                 | 29.6      |                               |                 |                                   |                        |                                   |                         |                 |
| 7  | [O III] ff $52\mu\text{m}/88\mu\text{m}$                                | 35.1      | $\lesssim 1.38/\lesssim 2.59$ | 1.97/2.83       | 1.68/2.68                         |                        | 6.15/3.74                         |                         |                 |
| 8  | [Ar IV] nn $\lambda 4740/\lambda 4711$                                  | 40.7      | 1.02/3.65                     | 0.871/3.27      |                                   | 1.31/3.84              | 1.98/4.22                         |                         |                 |
| 9  | [Ne V] ff $24.3\mu\text{m}/14.3\mu\text{m}$                             | 97.1      | 1.21 <sup>b</sup>             |                 |                                   |                        |                                   |                         |                 |
| 10 | Balmer decrement  |           | $\lesssim 4.00$               | $\lesssim 4.00$ | $\lesssim 4.00$                   | $\lesssim 4.00$        | $\lesssim 5.00$                   |                         |                 |
|    | $N_e(\text{CEL})$   |           | /3.65                         | /3.30           | /3.08                             | /3.64                  | /4.18                             |                         |                 |
|    | Extinction $c(\text{H}\beta)$   |           | 0.51 <sup>c</sup>             | 0.26            | 0.70                              | 0.13                   | 0.48                              |                         |                 |
| ID | Diagnostic ratio  | I.P. (eV) | NGC 6720                      | NGC 6741        | NGC 6781                          | NGC 6790               | NGC 6826                          | NGC 6884                | NGC 7662        |
|    |   |           |                               |                 |                                   |                        |                                   |                         |                 |
|    |   |           |                               |                 |                                   |                        | Ratio/ $T_e(10^3 \text{ K})$      |                         |                 |
| 1  | [S II] na   | 10.4      | 9.84/9.60                     | 3.15/10.0       | 11.7/9.54                         | 0.586/ <sup>d</sup>    |                                   | 1.50/17.0               | 2.93/15.3       |
| 2  | [O II] na   | 13.6      | 35.5/10.2                     | 9.47/12.5       | 43.9/10.3                         | 1.51/ <sup>d</sup>     | 14.8/12.0                         | 7.02/12.5               | 8.63/15.3       |
| 3  | [N II] na   | 14.5      | 84.7/10.2                     | 64.8/10.9       | 78.4/10.6                         | 22.7/18.0              | 79.1/10.3                         | 52.5/11.8               | 50.5/12.6       |
| 4  | [S III] fa  | 23.3      | 24.0/10.3                     | 7.39/13.9       |                                   |                        | 20.7/10.1                         | 9.62/11.7               | 11.2/11.6       |
| 5  | [Ar III] fn   | 27.6      |                               | 0.273/23.8      |                                   | 0.191/ <sup>d</sup>    | 0.439/13.9                        | 0.564/11.2              | 0.513/12.3      |
| 6  | [Ar III] na   |           | 164./10.5                     | 132./14.1       |                                   | 91.6/13.4              | 256./9.00                         | 151./10.9               | 96.8/13.2       |
| 7  | [O III] na  | 35.1      | 44.0/10.6                     | 26.7/12.6       | 50.7/10.2                         | 22.4/12.8              | 67.1/9.37                         | 37.8/11.0               | 23.3/13.4       |
| 8  | [O III] fa  |           | 0.916/10.8                    | 10.4/24.1       |                                   | 63.5/12.7 <sup>e</sup> | 1.08/9.87                         | 5.54/20.0               | 2.28/13.4       |
| 9  | [Ne III] fa   | 41.0      |                               | 0.762/12.5      |                                   | 0.339/15.4             | 1.71/9.72                         | 0.568/13.7 <sup>f</sup> | 0.778/12.4      |
| 10 | [O IV] fu   | 54.9      |                               |                 |                                   |                        |                                   |                         | 22.1/14.0       |
| 11 | [Ne IV] nu  | 63.5      |                               | 146./13.2       |                                   |                        |                                   | 246./10.5               | 98.2/18.2       |
| 12 | Balmer jump   |           | /9.1                          | /15.3           |                                   | /15.0                  | /9.65                             | /11.6                   | /12.2           |
|    |   |           |                               |                 |                                   |                        | Ratio/ $\log N_e(\text{cm}^{-3})$ |                         |                 |
| 1  | [S II] nn   | 10.4      | 0.964/2.70                    | 1.74/3.71       | 0.822/2.33                        | 2.19/4.74              | 1.37/3.30                         | 1.88/3.96               | 1.52/3.52       |
| 2  | [O II] nn   | 13.6      | 0.957/2.81                    | 2.04/3.64       | 1.18/2.42                         | 2.45/4.17              | 1.48/3.29                         | 2.17/3.82               | 1.70/3.49       |
| 3  | [S III] ff  | 23.3      |                               | 0.595/3.30      |                                   |                        | 1.20/2.60                         |                         | 0.416/3.52      |
| 4  | [Cl III] nn   | 23.8      | 0.776/2.69                    | 1.37/3.71       | 0.731/2.33                        | 2.46/4.29              | 0.911/3.12                        | 1.42/3.72               | 0.987/3.28      |
| 5  | C III] uu   | 24.4      |                               |                 |                                   |                        | 0.711/3.41                        |                         | 0.746/3.67      |
| 6  | N III] uu   | 29.6      |                               |                 |                                   |                        |                                   |                         | 0.661/3.41      |
| 7  | [O III] ff  | 35.1      | 1.43/2.57                     | 4.81/3.54       | 1.45/2.57                         |                        | 2.61/3.00                         | 3.31/3.23               | 2.62/3.03       |
| 8  | [Ar IV] nn  | 40.7      | 0.799/3.04                    | 1.26/3.91       | 0.768/2.85                        | 4.07/4.87              | 0.932/3.40                        | 1.56/4.01               | 1.26/3.46       |
| 9  | [Ne III] ff <sup>g</sup>  | 41.0      |                               |                 |                                   | 17.7/4.60              |                                   |                         |                 |
| 10 | [Ne IV] uu <sup>h</sup>   | 63.5      |                               |                 |                                   |                        |                                   |                         | 1.13/3.54       |
| 11 | [Fe III] nn <sup>i</sup>  | 16.2      |                               |                 |                                   | 0.513/<5.35            |                                   | 0.394/<5.45             |                 |
| 12 | Balmer decrement  |           | $\lesssim 3.00$               | $\lesssim 5.00$ |                                   | $\lesssim 5.00$        | $\lesssim 4.00$                   | $\sim 4.00$             | $\lesssim 4.00$ |
|    | $N_e(\text{CEL})$   |           | /2.70                         | /3.71           | /2.38                             | /4.60                  | /3.30                             | /3.87                   | /3.51           |
|    | Extinction $c(\text{H}\beta)$   |           | 0.20                          | 1.15            | 1.13                              | 1.10                   | 0.06                              | 1.00                    | 0.18            |

Notes. <sup>a</sup>For diagnostic ratio [O III]  $\lambda 4959/88 \mu\text{m}$ . <sup>b</sup>Ratio outside the low-density limit. <sup>c</sup>Assuming a total-to-selective extinction ratio,  $R = 2.0$ . <sup>d</sup>Outside the high-temperature limit ( $\sim 25\,000 \text{ K}$ ). <sup>e</sup>For diagnostic ratio [O III]  $\lambda 4959/52 \mu\text{m}$ . <sup>f</sup>[Ne III]  $36.0 \mu\text{m}/\lambda 3868 = 0.092$ , which yields  $T_e = 10\,600 \text{ K}$ . <sup>g</sup>[Ne III]  $15.6 \mu\text{m}/36.0 \mu\text{m}$ . <sup>h</sup>[Ne IV]  $\lambda 2424/\lambda 2422$ . <sup>i</sup>[Fe III]  $\lambda 4881/\lambda 4658$ . The densities derived are upper limits because of possible contamination of the  $\lambda 4658$  feature by C IV  $\lambda 4658$ .



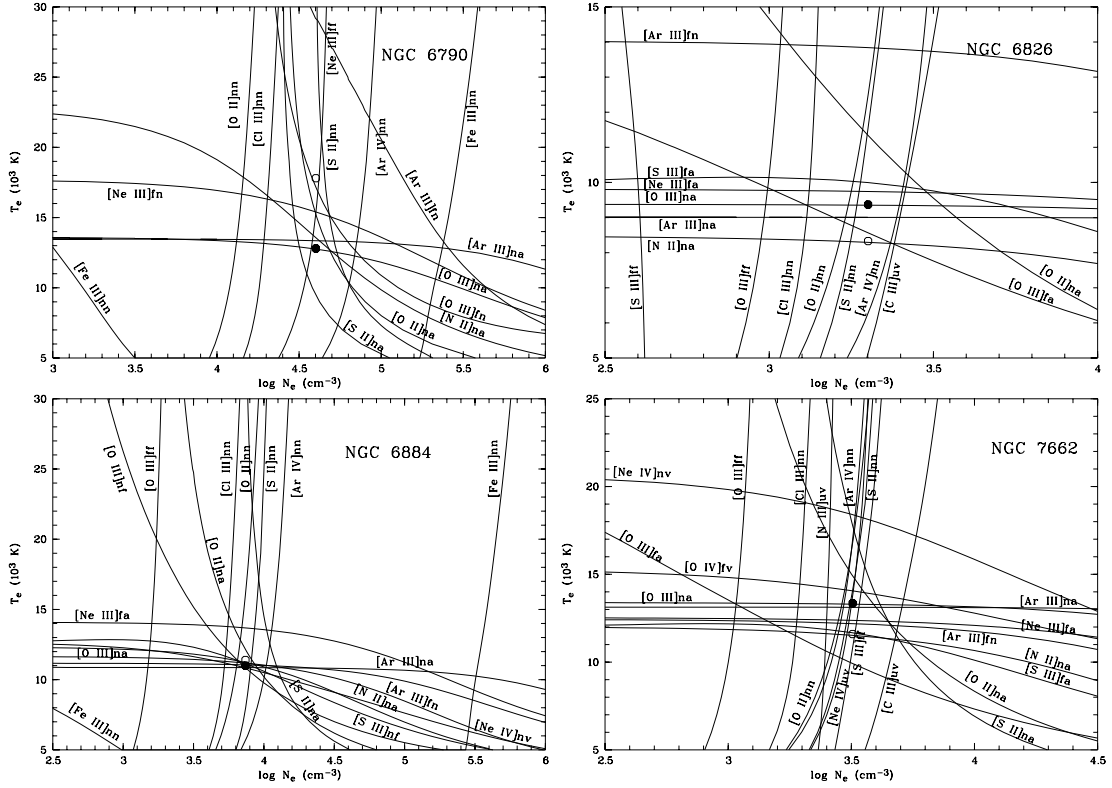


Figure 7 – continued

obtain electron temperatures and densities characteristic of individual excitation zones.

#### 4.1.1 Recombination excitation of the N II and O II auroral lines

The average  $T_e(\text{O III})$  for the whole sample is 11 800 K, about 560 K lower than the mean value of  $T_e(\text{N II})$ . For the 10 PNe in our sample for which both  $T_e(\text{O III})$  and  $T_e(\text{O II})$  have been determined, we find that, on average,  $T_e(\text{O III}) = 11\,800$  K, while  $T_e(\text{O II}) = 12\,700$  K, i.e. the latter is about 900 K higher. In an ionized nebula, singly ionized ionic species such as  $\text{N}^+$  and  $\text{O}^+$  normally form in the outer parts of the nebula outside the doubly ionized zone of  $\text{O}^{2+}$ . One expects that, in general, the electron temperature in this outer region of lower ionization degree should also be lower, contrary to what is observed.

A variety of hypotheses can be invoked to explain the observational result that  $T_e(\text{N II})$  and  $T_e(\text{O II})$  are systematically higher than  $T_e(\text{O III})$ . Radiation hardening in the nebular outer regions where singly ionized species exist can lead to a higher temperature in this region than in the inner, doubly ionized zone of  $\text{O}^{2+}$ . However, in this scenario, one expects that the effects would affect  $T_e(\text{N II})$  and  $T_e(\text{O II})$  by a nearly equal amount, given that  $\text{N}^0$  and  $\text{O}^0$  have very similar ionization potentials, and so do  $\text{N}^+$  and  $\text{O}^+$ . This is inconsistent with what is observed.

An alternative explanation is that both  $T_e(\text{N II})$  and  $T_e(\text{O II})$  have been overestimated because of the contamination of the [N II] and [O II] auroral lines,  $\lambda 5754$  and  $\lambda\lambda 7320, 7330$ , by recombination excitation. To quantify this effect, we use the expressions derived by Liu et al. (2000) to calculate the contributions of recombination to the observed intensities of the [N II]  $\lambda 5754$  and [O II]  $\lambda\lambda 7320, 7330$  lines,

**Table 8.** Effects of recombination excitation on temperatures derived from the [N II] and [O II] nebular to auroral line ratios. In the last two columns, values before and after ‘/’ are, respectively, temperatures derived before and after correcting for the effects of recombination excitation. In all cases,  $T_e$  derived from the nebular continuum Balmer discontinuity and  $\text{N}^{2+}/\text{H}^+$  and  $\text{O}^{2+}/\text{H}^+$  ionic abundance ratios from N II and O II ORLs, respectively, were adopted when estimating the contributions of recombination excitation, except for NGC 6781 where temperature and ionic abundance ratios derived from CELs were used.

| PN       | $T_e(\text{O III})$ | $T_e(\text{BJ})$ | $T_e(\text{N II})$ | $T_e(\text{O II})$ |
|----------|---------------------|------------------|--------------------|--------------------|
| Hu 1–2   | 19 500              | 18 900           | 13 000/13 000      | 15 600/15 600      |
| IC 3568  | 11 400              | 9490             | 17 800/12 100      | 16 600/13 300      |
| NGC 40   | 10 600              | 7020             | 8380/8310          | 8680/8630          |
| NGC 6210 | 9680                | 9300             | 11 100/10 500      | 13 200/13 100      |
| NGC 6572 | 10 600              | 11 000           | 13 600/13 400      |                    |
| NGC 6720 | 10 600              | 9100             | 10 200/10 200      | 10 200/9940        |
| NGC 6741 | 12 600              | 15 300           | 10 900/10 900      | 12 500/12 400      |
| NGC 6781 | 10 200              |                  | 10 600/10 600      | 10 300/10 200      |
| NGC 6790 | 12 800              | 15 000           | 18 000/17 800      |                    |
| NGC 6826 | 9370                | 9650             | 10 300/8330        | 12 000/11 500      |
| NGC 6884 | 11 000              | 11 600           | 11 800/11 400      | 12 500/12 800      |
| NGC 7662 | 13 400              | 12 200           | 12 600/11 600      | 15 300/15 300      |
| Mean     | 11 800              | 11 700           | 12 360/11 500      | 12 700/12 300      |

$$\frac{I_{\text{R}}(\lambda 5754)}{I(\text{H}\beta)} = 3.19t^{0.30} \frac{\text{N}^{2+}}{\text{H}^+}, \quad (1)$$

$$\frac{I_{\text{R}}(\lambda 7320 + \lambda 7330)}{I(\text{H}\beta)} = 9.36t^{0.44} \frac{\text{O}^{2+}}{\text{H}^+}. \quad (2)$$

where  $t \equiv T_e/10^4$ .

We use  $T_e(\text{BJ})$  (see Table 7) and  $\text{N}^{2+}/\text{H}^+$  and  $\text{O}^{2+}/\text{H}^+$  abundance ratios derived respectively from  $\text{N II}$  and  $\text{O II}$  ORLs (see Paper II) to estimate  $I_R(\lambda 5754)$  and  $I_R(\lambda 7320 + \lambda 7330)$ . We find that only for IC 3568 are the contributions of recombination excitation significant.

After corrections,  $T_e(\text{N II}) = 12\,100\text{ K}$  and  $T_e(\text{O II}) = 13\,300\text{ K}$ , which are, respectively, 5700 and 3300 K lower than the corresponding values before corrections. For the other PNe, the effects of recombination excitation on  $T_e(\text{N II})$  and  $T_e(\text{O II})$  are found to be

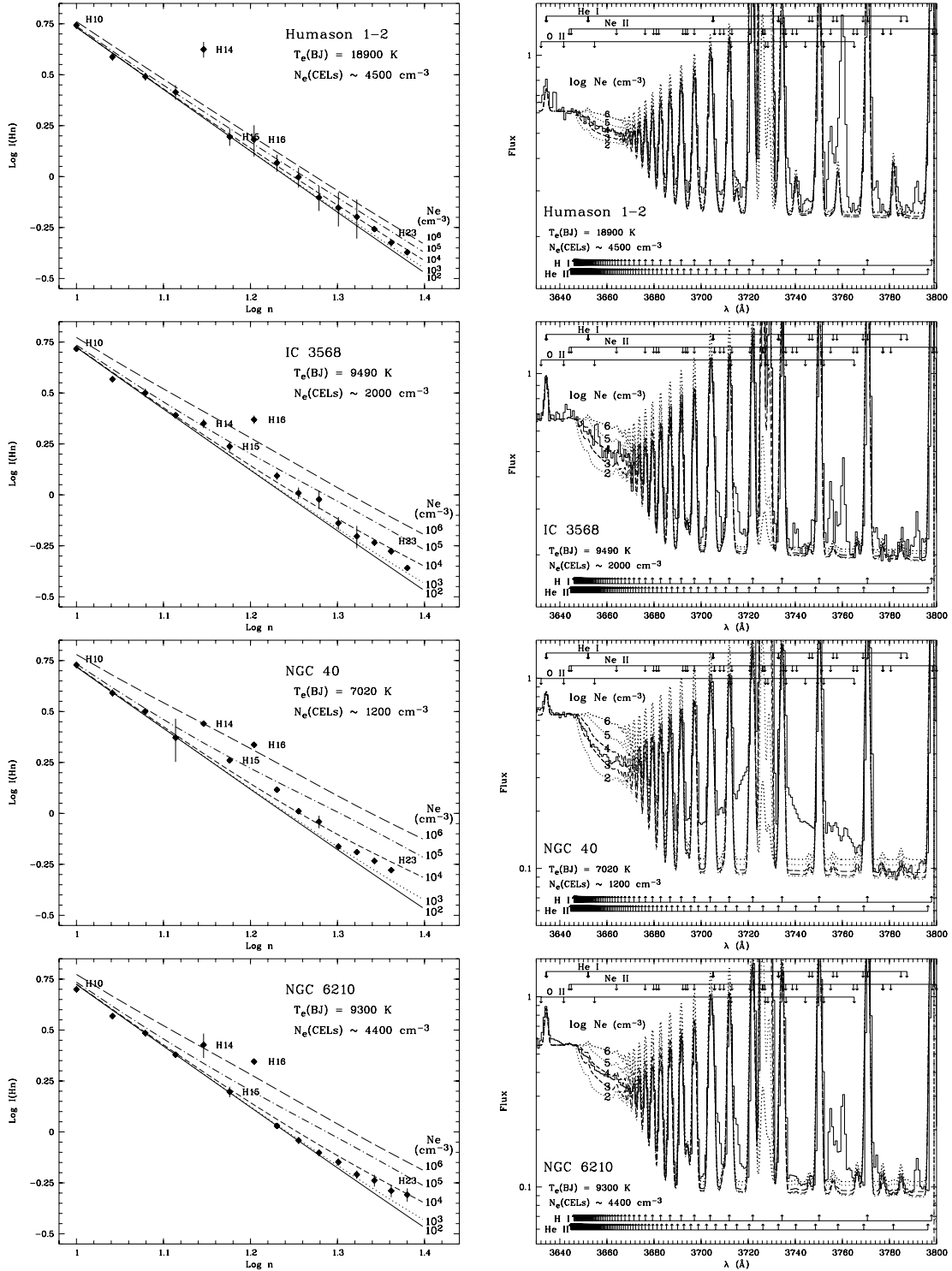


**Figure 8.** Left panel: observed intensities [in units where  $I(\text{H}\beta) = 100$ ] of high-order Balmer lines ( $n \rightarrow 2$ ,  $n = 10, 11, \dots, 24$ ) against the principal quantum number  $n$  of the upper level of the transition. Overplotted are curves showing the predicted values for electron densities ranging from  $N_e = 10^2$  to  $10^6\text{ cm}^{-3}$ . H 14–16 are affected by line blending. Right panel: dereddened spectra [in units where  $I(\text{H}\beta) = 100$ ] from 3630 to 3800 Å overplotted with synthetic spectra calculated assuming the Balmer jump temperature and a range of densities. H I Balmer lines and He II Pickering lines up to  $n = 500$  were included in the calculations. Each diagram is labelled by the nebular name, the Balmer jump temperature and the average electron density derived from CELs.

less than 5 per cent. We summarize our results in Table 8. For the  $[\text{N II}]$  diagnostic ratio, the contributions of recombination excitation to the observed intensities of the  $\lambda\lambda 6548, 6584$  nebular lines have also been corrected for.

PNe are known to show moderate density inhomogeneities (e.g. Liu et al. 2001a). Given the relatively low critical densities of the  $[\text{N II}]$  and  $[\text{O II}]$  nebular lines compared to those of the auroral lines,

the presence of density inhomogeneities can also lead to over-estimated temperatures derived from the  $[\text{N II}]$  and  $[\text{O II}]$  nebular line ratios (Viegas & Clegg 1994). This effect is however difficult to quantify and will not be discussed further here. In Paper II, we will adopt the  $T_e(\text{N II})$  values deduced after correcting for the effects of recombination excitation when calculating ionic abundances of singly ionized species.

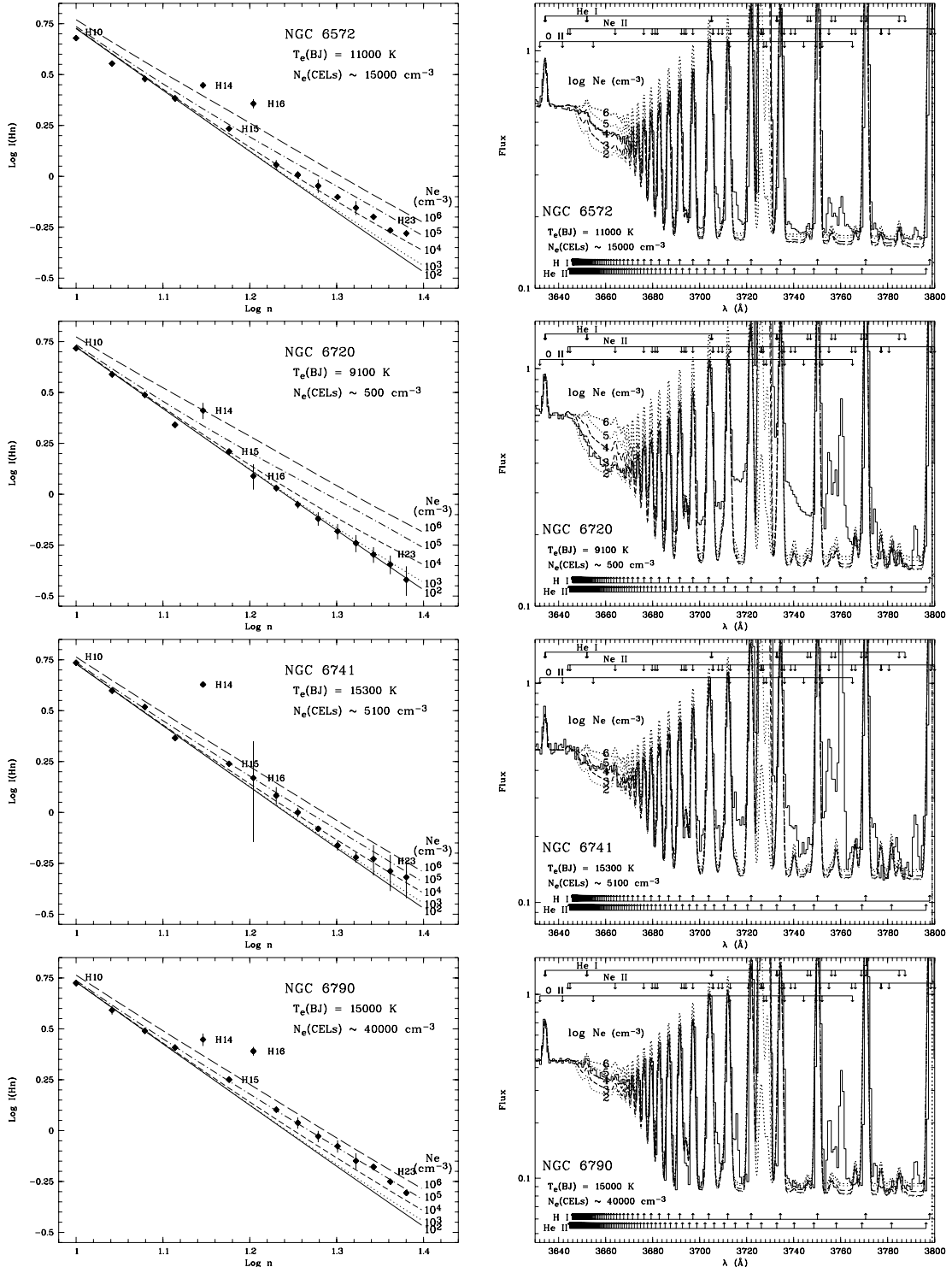


Figure 8 – continued

## 4.2 Recombination lines and continua

### 4.2.1 Balmer discontinuity and electron temperatures

From our deep scanned spectra, we were able to determine the nebular continuum Balmer discontinuity for all PNe except for NGC 6781. They were measured by modelling the observed continuum flux on either side of the discontinuity using low-order polynomials. Values of the electron temperature,  $T_e(\text{BJ})$ , deduced from the ratio of the nebular continuum Balmer discontinuity to H 11, are included in Table 7.  $T_e(\text{BJ})$  can be derived using the formula given in Liu et al. (2001b)

$$T_e(\text{BJ}) = 368 \times (1 + 0.259y^+ + 3.409y^{++}) \left( \frac{\text{BJ}}{\text{H11}} \right)^{-1.5} \text{ K},$$

where BJ/H 11 is in units of  $\text{\AA}^{-1}$  and  $y^+$  and  $y^{++}$  are helium ionic abundance ratios,  $y^+ \equiv \text{He}^+/\text{H}^+$  and  $y^{++} \equiv \text{He}^{++}/\text{H}^+$ . BJ/H 11  $\equiv [I_c(\lambda 3643) - I_c(\lambda 3681)]/I(\text{H}11)$ , where  $I_c(\lambda)$  represents the nebular continuum flux density per  $\text{\AA}$  at wavelength  $\lambda$ . The formula

was based on the effective recombination coefficients for H I recombination lines calculated by Storey & Hummer (1995) and the emissivities of H I, He I and He II recombination continua calculated by Brown & Mathews (1970). The wavelength 3681  $\text{\AA}$  is chosen in order to include a weak discontinuity of He I at 3678  $\text{\AA}$  produced by recombinations of free electrons to the He I  $2p^1P^o$  level (see Liu & Danziger 1993), which is inseparable from the H I Balmer discontinuity at 3646  $\text{\AA}$ . In practice, the nebular continuum flux at this wavelength is normally determined by fitting the continuum level at longer wavelengths and then extrapolated to shorter wavelengths. In this particular work,  $T_e(\text{BJ})$  was determined by fitting the synthesized nebular spectrum to the observed one. Note that, given the small wavelength span between the Balmer discontinuity at 3646  $\text{\AA}$  and H 11 at 3770  $\text{\AA}$ ,  $T_e(\text{BJ})$  derived from BJ/H 11 is nearly independent of extinction corrections.

The reason that  $T_e(\text{BJ})$  derived from BJ/H 11 has a weak dependence on  $y^+$  and  $y^{++}$  is because, apart from the H I Balmer discontinuity at 3646  $\text{\AA}$ , the  $\lambda\lambda 3643\text{--}3681$  wavelength region also contains a He II discontinuity at 3645  $\text{\AA}$  produced by  $\text{He}^{++}$  recombinations to

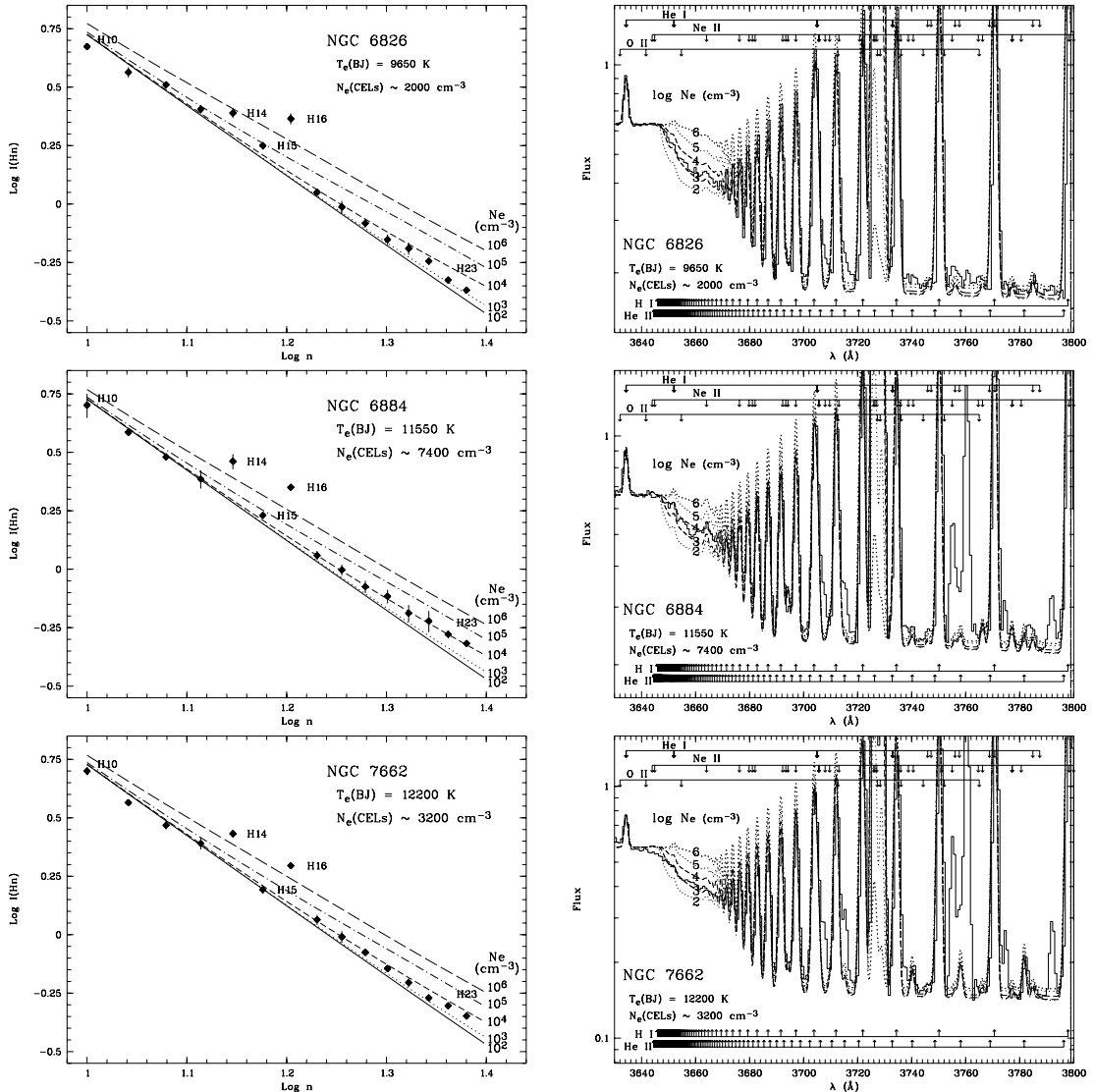


Figure 8 – continued

the He II  $n = 4$  bound level and a weak He I discontinuity at 3678 Å produced by recombinations of He<sup>+</sup> to the He I 2p<sup>1</sup>P level. Values of  $y^+$  and  $y^{++}$  used to calculate  $T_e$  (BJ) were derived from helium recombination lines such as He I  $\lambda 4471$ ,  $\lambda 5876$  and  $\lambda 6678$  for  $y^+$  and He II  $\lambda 4686$  for  $y^{++}$ , and will be presented in Paper II. Because  $y^+$  and  $y^{++}$  derived from the helium recombination lines also have a weak dependence on electron temperature, the process was iterated until self-consistent values for  $y^+$  and  $y^{++}$  and  $T_e$ (BJ) were achieved.

#### 4.2.2 Balmer decrement and electron densities

Intensities of high-order Balmer lines ( $n \geq 10$ ) relative to a low-order Balmer line (e.g. H $\beta$ ) are sensitive to electron density and thus can be used as a density-diagnostic (Liu et al. 2000). In Fig. 8, the observed intensities of high-order Balmer lines  $n \rightarrow 2$ ,  $n = 10, 11, \dots, 23$ , are plotted against the principal quantum number  $n$  of the upper level of the transition. H 14 at 3721.94 Å is blended with the [S III]  $\lambda 3721.63$  line and H 16 at 3703.86 Å is partially blended with He I  $\lambda 3705.12$ . The intensity of H 16 has to be retrieved using multiple Gaussian line profile fits which are not always reliable. Finally, H 15 at 3711.97 Å seems to be affected by blending with an unknown feature. The curves overplotted give predicted values for a range of electron densities (Storey & Hummer 1995).

The right columns of Fig. 8 plot the dereddened spectra around the Balmer jump wavelength region. The observed spectra are compared to synthetic spectra calculated for a range of densities, assuming the Balmer jump temperature  $T_e$ (BJ) (see Table 7), except for NGC 6781 where the temperature derived from the [O III] nebular to auroral line ratio,  $T_e$ (O III), was used. In calculating the synthetic spectra, we have included contributions from lines of the H I Balmer series and He II Pickering series up to  $n = 500$ . ORLs of He I, Ne II and O II that fall in the wavelength range were also included, with their intensities calculated using the ionic abundances deduced in Paper II. The lines are marked in the panel for each PN.

Fig. 8 shows that, for all nebulae in our sample, the bulk of hydrogen emission arises from regions with electron densities comparable to values derived from various forbidden-line density-diagnostics, and there is no evidence of a substantial amount of ionized high-density ( $N_e \gtrsim 10^6 \text{ cm}^{-3}$ ) material in these nebulae, unless such material is also hydrogen-deficient (Liu et al. 2000). The upper limit on electron density implied by the observed intensities of high-order Balmer lines for each nebula is listed in Table 7.

In Paper II we will use the line fluxes and nebular plasma diagnostic results presented in the current paper to carry out a detailed abundance analysis, using both strong CELs and much weaker heavy elemental ORLs in order to contrast the results derived from these two types of emission line. We will investigate whether the phenomenon previously observed for a limited number of PNe, whereby ORL heavy element abundances are systematically higher than those derived from the traditional method based on CELs, also occurs for the current sample of PNe, and, if so, the magnitudes and distribution of the discrepancies, their possible links to other nebular properties, and the possible physical causes of the discrepancies.

#### ACKNOWLEDGMENT

We would like to thank Dr R. Rubin for a critical reading of the manuscript prior to its submission.

#### REFERENCES

- Acker A., Marcout J., Ochsenbein F., Stenholm B., Tylenda R., 1992, Strasbourg–ESO Catalogue of Galactic Planetary Nebulae. Parts 1 and 2 (A92)
- Aller L. H., Czyzak S. J., 1979, Ap&SS, 62, 397 (AC79)
- Aller L. H., Czyzak S. J., 1983, ApJS, 51, 211 (AC83)
- Aller L. H., Keyes C. D., 1987, ApJS, 65, 405 (AK87)
- Barker T., 1978, ApJ, 219, 914 (B78)
- Benjamin R. A., Skillman E. D., Smits D. P., 1999, ApJ, 514, 307
- Brown R. L., Mathews W. G., 1970, ApJ, 160, 939
- Cahn J. H., Kaler J. B., Stanghellini L., 1992, A&AS, 94, 399 (CKS92)
- Cardelli J. A., Clayton G. C., Mathis J. S., 1989, ApJ, 345, 245
- Carrasco L., Serrano A., Costero R., 1983, Rev. Mex. Astron. Astrofis., 8, 187 (CSC83)
- Clegg R. E. S., Seaton M. J., Peimbert M., Torres-Peimbert S., 1983, MNRAS, 205, 417
- Condon J. J., Kaplan D. L., 1998, ApJS, 117, 361 (CK98)
- Feibelman W. A., 1999, ApJ, 514, 296
- Greenstein J. L., 1981, ApJ, 245, 124
- Grewing M. et al., 1978, Nat, 275, 394
- Groves B., Dopita M. A., Williams R. E., Hua C., 2002, PASA, 19, 425
- Harrington J. P., 1996, in Jeffery C. S., Heber U., eds, ASP Conf. Ser. Vol. 96, Hydrogen-Deficient Stars. Astron. Soc. Pac., San Francisco, p. 193
- Howarth I. D., 1983, MNRAS, 203, 301
- Kaler J. B., 1983, ApJ, 264, 594 (K83)
- Kisielius R., Storey P. J., 2002, A&A, 387, 1135
- Kwok S., 1994, PASP, 106, 344
- Larson K. A., Whittet D. C. B., Hough J. H., 1996, ApJ, 472, 755
- Lester D. F., Dinerstein H. L., 1984, ApJ, 281, L67
- Liu X.-W., 2002, Rev. Mex. Astron. Astrofis. Ser Conf., 12, 70
- Liu X.-W., 2003, in Kwok S., Dopita M., Sutherland R., eds, Proc. IAU Symp. 209, Planetary Nebulae: their Evolution and Role in the Universe. Astron. Soc. Pac., San Francisco, p. 339
- Liu X.-W., Danziger I. J., 1993, MNRAS, 263, 256
- Liu X.-W., Storey P. J., Barlow M. J., Clegg R. E. S., 1995, MNRAS, 272, 369
- Liu X.-W., Storey P. J., Barlow M. J., Danziger I. J., Cohen M., Bryce M., 2000, MNRAS, 312, 585
- Liu X.-W. et al., 2001a, MNRAS, 323, 343
- Liu X.-W., Luo S.-G., Barlow M. J., Danziger I. J., Storey P. J., 2001b, MNRAS, 327, 141
- Liu Y., Liu X.-W., Barlow M. J., Luo S.-G., 2004, MNRAS, in press (doi:10.1111/j.1365-2966.2004.08156.x) (Paper II) (this issue)
- Middlemass D., 1990, MNRAS, 244, 294
- Milne D. K., Aller L. H., 1975, A&A, 38, 183
- O’Dell C. R., 1963, ApJ, 138, 1018 (O63)
- Peimbert M., 1967, ApJ, 150, 825
- Peimbert M., Torres-Peimbert S., 1971, Bol. Obs. Tonantzintla Tacubaya, 6, 21 (PTP71)
- Perinotto M., 1974, A&A, 35, 293 (P74)
- Pottasch S. R., Beintema D. A., Bernard Salas J., Feibelman W. A., 2001, A&A, 380, 684 (P2001)
- Pottasch S. R., Hyung S., Aller L. H., Beintema D. A., Bernard-Salas J., Feibelman W. A., Klöckner H.-R., 2003a, A&A, 401, 205 (P03)
- Pottasch S. R., Bernard-Salas J., Beintema D. A., Feibelman W. A., 2003b, A&A, 409, 599 (P2003)
- Rowlands N., Houck J. R., Skrutskie M. F., Shure M., 1993, PASP, 105, 1287
- Rubin R. H., 1989, ApJS, 69, 897
- Rubin R. H., Colgan S. W. J., Haas M. R., Lord S. D., Simpson J. P., 1997, ApJ, 479, 332
- Ruiz M. T., Peimbert A., Peimbert M., Esteban C., 2003, ApJ, 595, 247
- Sabbadin F., Cappellaro E., Turatto M., 1987, A&A, 182, 305

- Seaton M. J., 1979, *MNRAS*, 187, 785  
Siódmiak N., Tylenda R., 2001, *A&A*, 373, 1032 (ST01)  
Storey P. J., Hummer D. G., 1995, *MNRAS*, 272, 41  
Tsamis Y. G., Barlow M. J., Liu X.-W., Danziger I. J., Storey P. J., 2003, *MNRAS*, 345, 186  
Tsamis Y. G., Barlow M. J., Liu X.-W., Storey P. J., Danziger I. J., 2004, *MNRAS*, in press  
Viegas S. M., Clegg R. E. S., 1994, *MNRAS*, 271, 993  
Walton N. A., Barlow M. J., Clegg R. E. S., 1993, in Dejonghe H., Habing H.J., eds, *Proc. IAU Symp. 153, Galactic Bulges*. Kluwer, Dordrecht, p. 337  
Welty D. E., Fowler J. R., 1992, *ApJ*, 393, 193  
Wyse A. B., 1942, *ApJ*, 95, 356 (W42)

This paper has been typeset from a  $\text{\TeX}/\text{\LaTeX}$  file prepared by the author.